Physics of Complex Systems

PHYSICS OF COMPLEX SYSTEMS

CONTENTS

Dielectric polarisation in naturally disordered trilead tetroxide Pb_3O_4

V. T. Avanesyan[✉1], E. P. Baranova[1], K. A. Chursina[1]

[1] Herzen State Pedagogical University of Russia, 48 Moika River Emb., Saint Petersburg 191186, Russia

Authors

Vachagan T. Avanesyan, e-mail: avanesyan@mail.ru, ORCID: 0000-0001-5772-8375

Ekaterina P. Baranova

Ksenia A. Chursina

Abstract. The paper presents the results of an experimental study of trilead tetraoxide Pb_3O_4 binder layers and their dielectric properties. The study revealed polarisation processes in low frequency range associated with structure peculiarities in the Pb_3O_4 compound. The study established the dependence of dielectric properties on temperature and frequency of the applied field. The complex dielectric response of layer samples was measured under various AC drive and DC bias conditions. The paper provides an explanation for the influence of the simultaneous AC and DC voltages on dipole and Maxwell–Wagner polarisation in Pb_3O_4. It is assumed that there is an impact of interfacial barriers in the polycrystalline structure. The paper discusses the role of lone pair (LP) electrons Pb^{2+} in polarisation properties of trilead tetraoxide compound.

Keywords: Pb_3O_4, dielectric polarisation, Maxwell–Wagner polarisation, polycrystalline structure, dielectric response.

Introduction

Electret materials mentioned in literature include two major types, i.e. organic polymers and inorganic dielectrics (Sessler 1987). Although organic materials such as Teflon show excellent electret properties when applied to microphones, their fabrication is still scarce and hardly compatible with the integrated–circuit technology. In recent years, inorganic oxide materials have been widely investigated to solve this problem. A long-standing interest of researchers, who have been studying the lead oxide system over the last decades, reflects its technical value as well as its complex and still unclear physical behaviour.

The trilead tetraoxide composition has attracted considerable interest recently due to its high resistance with large density of deep traps suggesting that this material is suitable for electret applications. Moreover, a practically interesting problem lies in the fact that polarisation and conductivity in this oxide system are closely connected with electret and photoelectric properties (Avanesyan 1999; Avanesyan et al. 1999; Avanesyan et al. 2002).

The high–resistivity lead oxide electret systems with Pb^{2+} cations are of interest as well because their $6s^2$ LP electrons cause asymmetric oxygen coordination, often resulting in acentric or even polar crystal structures. According to Galy et al. (Galy et al. 1975), the LP is an intermediate state between an inert spherical ns^2–type orbital, which is centred on the nucleus, and a non-bonded hybridised–orbital lobe, which is not spherical but localised far from the atomic nucleus. This orbital of two electrons is encountered in compounds containing ions with an appropriate valence.

The present work deals with the study of dielectric properties and AC conductivity of the Pb_3O_4 binder layers. The study explore the possibility of using the LP concept for a better understanding of polarisation properties of trilead tetraoxide.

Experiment

Fine powder of Pb_3O_4 was added to organic-silicon binder and stirred vigorously to make a homogeneous suspension. Then it was placed between a clean aluminium plate and an aluminium film by successive evaporation to form a cell for capacitance measurement. The experimental samples had a thickness of 50...100 micrometers. Dielectric dispersion was studied by using a precision impedance meter E7-20 with measuring voltage U = 0.04 V. Dielectric measurements of polycrystalline Pb_3O_4 binder layers were performed in the frequency range f = 10...10^6 Hz.

The mentioned device was used for AC conductivity measurement as well. The samples were mounted in a dark chamber that could be evacuated in order to control the sample environment, which was found extremely important for the reproducibility of the experimental results. The heating of samples in an interval of temperatures T = 293...400 K was carried out with a rate of about 1.5 K/min. Temperature was measured with a calibrated copper–constantan thermocouple.

Results and discussion

In practice, the dielectric is often subjected to the simultaneous action of AC and DC voltages (Rapos, Calderwood 1974). Such study can be useful from a practical point of view. It can also provide additional characterisation of dielectric polarisation. Such experimental measurements were carried out in this study. The typical results of the observed fractional change variation in capacitance (correspondingly in dielectric permittivity) and dielectric losses (tanδ) with temperature at constant frequency of the applied field f = 10^3 Hz are presented in Fig. 1, 2.
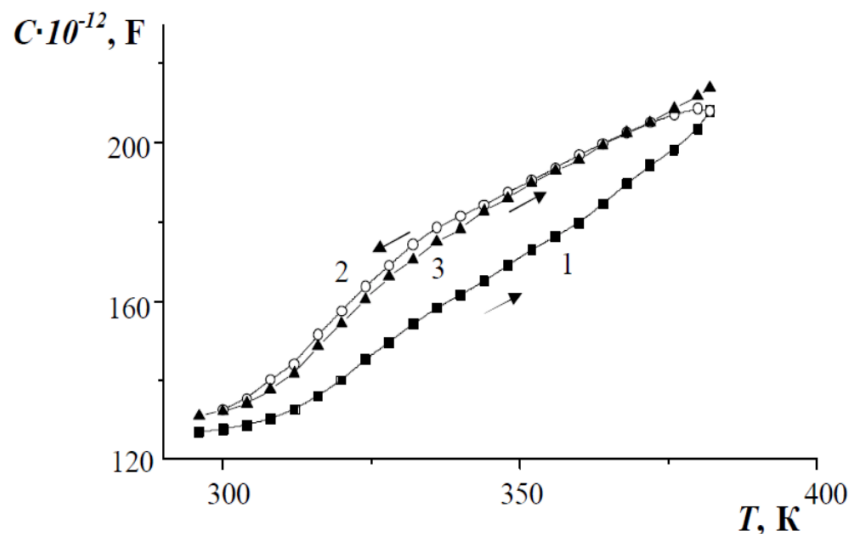
Fig. 1. Temperature dependence of Pb_3O_4 binder layer capacitance without (curves 1, 2) and with additional bias voltage U_{dc} = 10 V (curve 3). Arrows specify the direction of temperature change when heated or cooled

The findings indicate that the values of C increase very slowly at low temperatures. As the temperature rises, the values of C increase relatively rapidly towards higher temperatures. The application of AC voltage to Pb_3O_4 layer samples reaches a peak in the tanδ vs. temperature dependence near 325 K, accompanied by an increase in C and tanδ, and shifts to low temperature when DC voltage is simultaneously applied. The results of dielectric measurements on polycrystalline samples of the Pb_3O_4 compound showed thermal hysteresis caused by changes occurring in the grain boundaries during thermal cycling.

Electrical conduction in Pb_3O_4 binder layers also shows marked dispersion with temperature. The activation energy ΔE for conductivity relaxation was evaluated from the f c vs. 1000/T log plot and made up the value of ΔE = 0,56 eV (for temperatures below T = 320 K) and ΔE = 0,02 eV (for temperatures above T = 320 K).
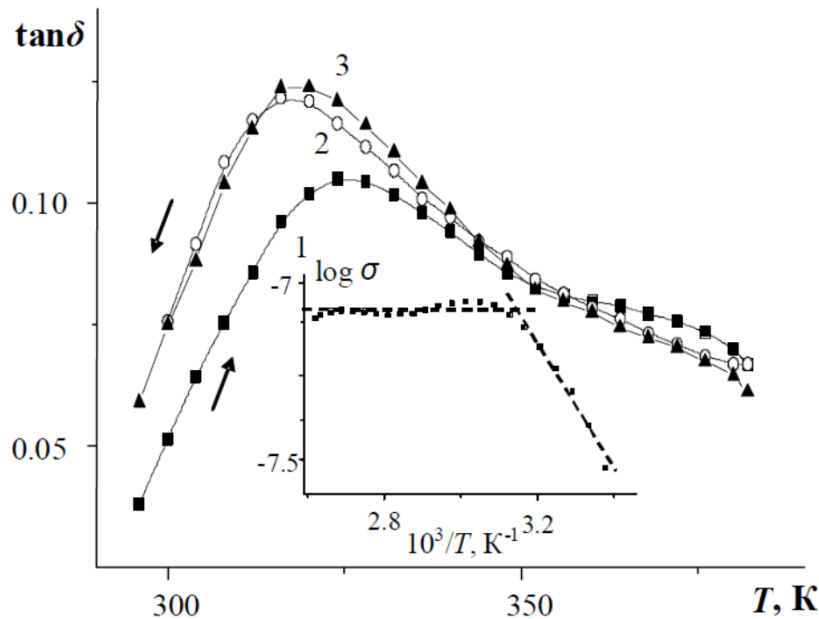
Fig. 2. The tanδ temperature dependence of Pb_3O_4 binder layers with (curve 3) and without (curves 1, 2) additional bias voltage U_{dc} =10 V. Arrows specify the direction of temperature change when heated or cooled. The insert shows the temperature dependence on the AC conductivity

The dielectric permittivity, as calculated from the measured capacitance and losses (tanδ) of Pb_3O_4 layer structures in an investigated range of frequencies, exhibited strong frequency dependence (Fig. 3). The influence of the frequency factor indicates the relaxation nature of dielectric polarisation. It is possible to assume that this is an "apparent" permittivity influenced by the density distribution of charge carriers.
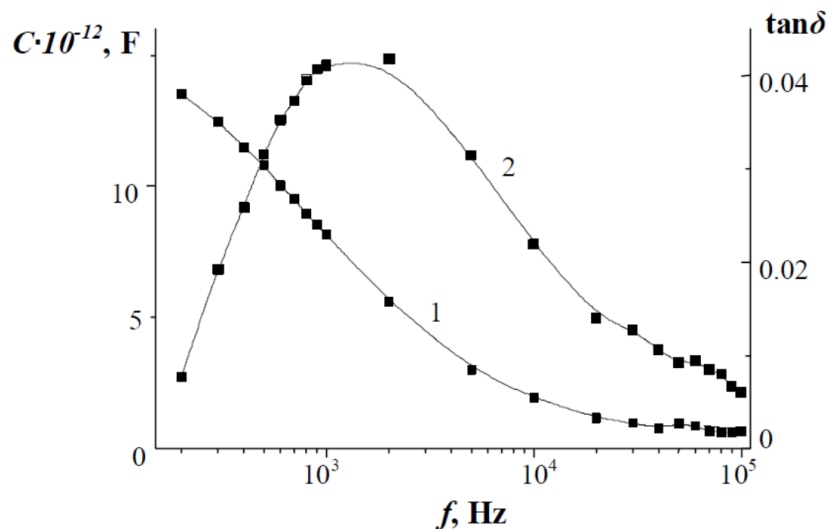
Fig. 3. Frequency dependence of the Pb_3O_4 binder layer capacitance (curve 1) and tanδ (curve 2) at T = 293 K

The imposition of AC and DC electric field possibly causes the deformation of an intergranular potential barrier and by that the orientation of the charged particles in primary direction occurs. The number of particles detained by barriers can change, thus decreasing the total dipole moment of the relaxing particles system. The average magnitude of the angle that the dipole makes with the applied field is reduced by the presence of a DC field. The torque, which an applied AC field is able to exert on the dipole, is thereby reduced; therefore, the polarisation brought from the given AC field is smaller in the presence of a DC field.

The results outlined above can be explained also on the basis of space charge formation near the barriers of polycrystalline structure. A possible reason for this behaviour of dielectric parameters may be the presence of some number of trapped electrons in defect states. The migration of the polycrystalline structure defects in an electrical field modulates an interface potential barrier and can influence the formation of a spatial charge. The presence of a DC field and an AC field at the same time causes an asymmetrical barrier. The structure defects migration of the polycrystalline Pb_3O_4 oxide composition related to the LP of Pb^{2+} cations modulates the intergranular barrier, and thus may have a marked effect on the formation of a spatial charge.

The growth of the energy barrier ΔE increases relaxation time in accordance with the formula $\tau = \tau_o e^{\Delta E/kT}$ and causes the shift of the tanδ peak to low temperatures. It can be concluded that dielectric relaxation is caused by jumping of particles (electrons or ions) between nearest-neighbour sites under AC electric field and that successive jumping between nearest-neighbour sites under DC electric field causes DC conduction.

The strong correlation between conductance and capacitance in the frequency range under investigation can be demonstrated by plotting Cole–Cole plot of Ctanδ vs. C over the appropriate frequency range (Fig. 4) with frequency as a parameter. It seems reasonable to say that the observed low frequency dispersion is the result of non–Debye relaxation mechanism with continuously distributed relaxation times. The AC conductivity at T = 293 K shows strong frequency dependence according to the relation $\sigma_{ac}(\omega) = A\omega^s$.
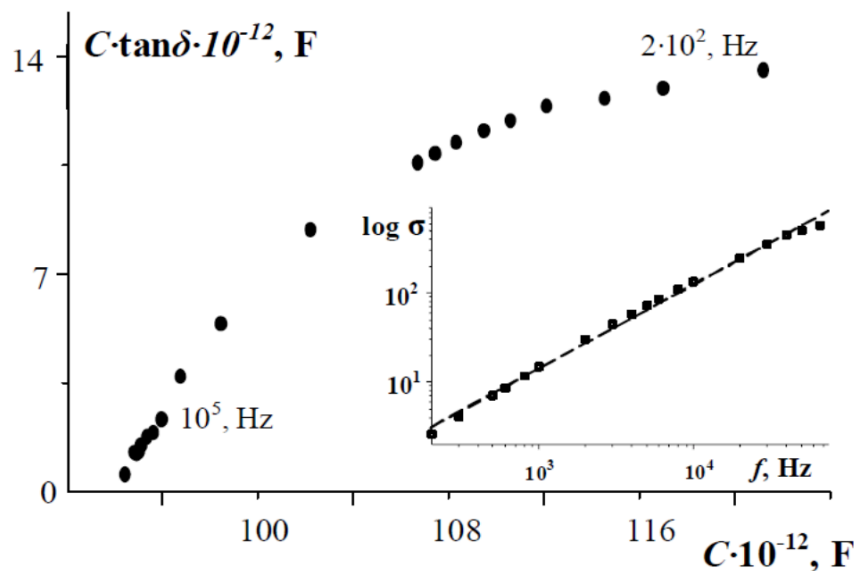
Fig. 4. Complex Cole–Cole plot of dielectric components for Pb_3O_4 binder layer. T = 293 K. The insert shows the frequency dependence of conductivity

The value of the exponent s obtained from the linearity of logσ against log f was found as 0.69 that can be dealt with the hopping mechanism.

In order to clarify the origin of dielectric dispersion observed in Pb_3O_4 layers, the equivalent circuit based on the Maxwell–Wagner model (Jonsher 1996) was investigated by taking into account the microstructure of samples. It is considered that the microstructure of Pb_3O_4 consists of Pb_3O_4 grains and intergranular layers where each Pb_3O_4 grain is three-dimensionally separated by this layer. The equivalent circuit for such an idealised model can be assumed as shown in Fig. 5a. The circuit consists of two blocks

of resistance and capacitance: R_1 and C_1 are resistance and capacitance of intergranular layer; R_2 and C_2 are resistance and capacitance of Pb_3O_4, respectively. The simplified equivalent circuit of the sample can be represented by a parallel R_C network as shown in Fig. 5b. Here each element C_e and R_e is defined experimentally and is connected to parameters of grains and intergranular layers by:

$$C_e = \frac{\omega^2 R_1^2 R_2^2 C_1 C_2 (C_1 + C_2) + R_1^2 C_1 + R_2^2 C_2}{\omega^2 R_1^2 R_2^2 (C_1 + C_2)^2 + (R_1^2 + R_2^2)^2}, \tag{1}$$

$$R_e = \frac{\omega^2 R_1^2 R_2^2 (C_1 + C_2)^2 + (R_1 + R_2)^2}{\omega^2 R_1 R_2 (R_1 C_1^2 + R_2 C_2^2) + R_1 + R_2}, \tag{2}$$

a)   b)
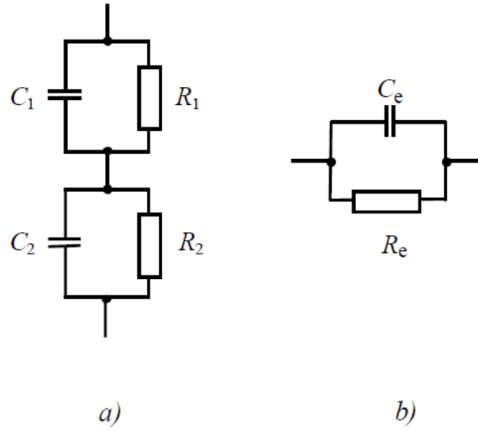
Fig. 5. Equivalent circuit model for Pb_3O_4 structure: *(a)* with an intergranular layer (R_1, C_1) and grain (R_2, C_2), *(b)* the simplified equivalent circuit

Equations (1) и (2) define frequency dependence of the sample capacity and resistance. To simplify the analysis of C_e and R_e (f) functions we can assume that $R_1 >> R_2$ in view of amorphous and crystal phase distinction. In the low temperatures region, the inequality and relations are fair:

$$\omega \tau_{1L} >> \omega \tau_{2L} >> 1, \tag{3}$$

where $\omega = 2\pi f, \tau_i = R_i C_i$;

$$C_{eL} = \frac{C_1 C_2}{(C_1 + C_2)}; \quad \frac{1}{R_{eL}} = G_2 \left(\frac{C_1}{C_1 + C_2}\right), \tag{4}$$

where $G_2 = \frac{1}{R_2}$ and the resistance R_{eL} is defined by crystal phase conductivity of a sample.
The high temperatures region can be described as:

$$1 >> \omega \tau_{2H} >> \omega \tau_{1H} \tag{5}$$

$$C_{eH} = C_1 \quad; \frac{1}{R_{eH}} = G_1, \tag{6}$$

where $G_1 = \frac{1}{R_1}$', but the capacity and the resistance of the sample are defined in parameters of an amorphous phase. The situation in the range of intermediate temperatures can be expressed as:

$$\omega \tau_1 >> 1 >> \omega \tau_2, \tag{7}$$

$$C_{eL} < C_{eH} < C_{e2}; \quad \frac{1}{R_{e2}} = G_1 + \left(\omega^2 C_1^2 / G_2\right). \tag{8}$$

In the latter the magnitude of C_e increases and the conductivity includes a component which decreases along with the temperature growth. This can also result in a positive factor of resistance. The positive resistance coefficient, in particular, may be attributed to the relaxation in barrier layers due to the formation of acceptor states on the surface of grains. It was found that Pb^{2+} in some materials could act as hole traps to give Pb^{3+} centers (Robertson et al. 1993). As a matter of fact, the parallel between structures and conductivities of Pb_3O_4 is striking; therefore, it supports the idea of the relationship between lone pair disposition and conductivity. The specified phenomenon within the framework of the discussed model is caused by the change of a ratio between active and reactive components of intergranular layer conductivity.

The inspection of the structure geometry in the oxide semiconductor in question shows that all cationic sites display typically distorted coordinations usually found in Pb^{2+} oxides, where the presence of localised $6s^2$ LP electrons determines the occurrence of short metal–oxygen interactions only on the opposite side with respect to $6s^2$ localised electrons. Chemical bonding in complexes with inert pair of ns^2 ions is largely determined by s–p mixing (Avanesyan 1999; Galy et al. 1975). Hence, the LP takes part in the chemical bonding and cannot be considered as an inert pair. Thus, the unshared ns^2 electron pair causes a tendency for the instability to antisymmetric distortions of lattice elements and their environment. The large defined value of the trilead tetraoxide dielectric constant ($\varepsilon{\sim}25$) is related to the high polarisability of Pb^{2+} cations in which the LP causes a non-spherical change of distribution around these cations.

Conclusion

The dielectric information is obtained, including electric characteristics of polycrystalline Pb_3O_4 binder layers. The influence of DC voltage bias on dielectric response of Pb_3O_4 layers in the temperature interval T= 293…400 K is established. Thus, the greatest changes occur at high temperatures and low frequencies of a measurement field. Experimental results and theoretical considerations suggest that the dielectric dispersion observed in polycrystalline Pb_3O_4 layers can be attributed to the nature of interlayer Maxwell–Wagner polarisation with a distribution of relaxation times.

Therefore, besides bond formation, non-bonding lone pairs can play a key role in determining polarisation properties of oxide semiconductors. This approach is sufficient for the molecular design of new electret materials and for the better understanding of electrets on a molecular scale.

References

Avanesyan, V. T. (1999) *Polyarizatsionnye yavleniya v estestvenno-neuporyadochennykh poluprovodnikakh s odinochnoj elektronnoj paroj [Polarization phenomena in naturally disordered semiconductors with a single electron pair]. PhD dissertation (Physics)*. Saint Petersburg, Herzen State Pedagogical University of Russia, 258 p. (In Russian)

Avanesyan, V. T., Bordovskii, V. A., Potachov, S. A. (1999) The polarization phenomena in a-PbO photoelectret ceramic. In: A. A. Konsta, A. Vassilikou-Dova, K. Vartzeli-Nikaki (eds.). *Proceedings of 10ᵗʰ International Symposium on electrets ISE 10. 22–24 September, 1999, European Cultural Centre of Delphi, Greece*. S. p.: IEEE, pp. 193–196. (In English)

Avanesyan, V. T., Bordovskii, V. A., Potachev, S. A. (2002) Dielectric characterization of the lone pair oxide structure. *Journal of Non-Crystalline Solids*, 305 (1–3), 136–139. DOI: 10.1016/S0022-3093(02)01090-6 (In English)

Galy, J., Meunier, G., Andersson, S., Åström, A. (1975) Stéréochimie des eléments comportant des paires non liées: Ge (II), As (III), Se (IV), Br (V), Sn (II), Sb (III), Te (IV), I (V), Xe (VI), Tl (I), Pb (II), et Bi (III) (oxydes, fluorures et oxyfluorures). *Journal of Solid State Chemistry*, 13 (1–2), 142–159. DOI: 10.1016/0022-4596(81)90157-2 (In French)

Jonscher, A. K. (1996) *Universal relaxation law*. London: Chelsea Dielectric Press, 415 p. (In English)

Rapos, M., Calderwood, J. H. (1974) Dielectric properties of MoO_3 under the simultaneous action of AC and DC voltages. *Journal of Physics D: Applied Physics*, 7 (13), article 1838. DOI: 10.1088/0022-3727/7/13/309 (In English)

Robertson, J., Warren, W. L., Tuttle, B. A., Dimos, D., Smyth, D. M. (1993) Shallow Pb^{3+} hole traps in lead zirconate titanate ferroelectrics. *Applied Physics Letters*, 63 (11), 1519–1521. DOI: 10.1063/1.110761 (In English)

Sessler, G. M. (ed.). (1987) *Electrets. Vol. 33*. Berlin; Heidelberg; New York: Springer Publ., 453 p. DOI: 10.1007/3-540-17335-8 (In English)

Relaxation methods for studying transformations in polymer systems

K. L. Levine[✉1], J. O. Iroh[2], D. E. Tallman[3]

[1] Telecommunication Academy named after S. M. Budyonny, 3 Tikhoretsky Ave., Saint Petersburg 194064, Russia
[2] University of Cincinnati, 2600 Clifton Ave., Cincinnati OH 45221, USA
[3] North Dakota State University, 1340 Administration Ave., Fargo ND 58105, USA

Authors

Kirill L. Levine, e-mail: levinkl@hotmail.com, ORCID: 0000-0002-1050-6609

Jude O. Iroh, ORCID: 0000-0003-0778-4023

Dennis E. Tallman

Abstract. It is known that self-organisation of nanostructures according to the bottom-up approach is driven by the competition of several processes: surface tension, diffusion, gravity, buoyant force and, perhaps, molecular coordination phenomenon. The last one was discussed in the 70s in terms of the so-called "mobile organised molecular arrays" and proved with the help of nuclear magnetic relaxation. This study shows examples of self-organised structures obtained electrochemically by authors and provides a discussion regarding the same terms.

Keywords: self-organisation, nuclear magnetic relaxation, polymers, relaxation processes, microcontainers.

Introduction

One of the most important ecological problems of the 21st century is plastic pollution. Using self-disposable (biodegradable and self-degradable) polymer containers can be a solution; therefore, creating smart recycling polymers is a matter of high priority. It is important to understand processes underlying polymerisation in order to create polymers with "smart" behaviour. One of such processes is self-organisation, which is taking place during polymerisation or cooling of the polymer melt.

Self-organisation resulting in growth of nanostructures is considered to be an example of the bottom-up approach as described in (Faynman 1960). Later ideologists of nanotechnology (Lehn 1988; Nicolis, Prigogine 1977) described self-organisation as competition between several forces: surface tension, diffusion, buoyant force, gravity and phenomena related to coordination, for example, atoms of transition elements and catalysis. These factors are responsible for the variety of forms appearing during polymerisation. Self-organisation in polymers occurs not only due to polymerisation of monomers but also due to the cooling of polymer and oligomer melts below glass transition temperature (T_c). It results in the appearance of peculiar formations, such as spherulites, lamellae and folds. It is believed that polymers demonstrate a specific mechanism of self-organisation that utilises the so-called "mobile organised molecular arrays" or "labile pre-pregs" (LP) (literal translation from Russian)—aggregation of monomers in the condition of chaotic movement (Gvozdetskii et al. 1968). Those arrays are capable of moving along the sample and responsible for morphological significances.

Relaxation methods

Fundamentals of relaxation processes in liquid dielectrics and melts are based on hydrodynamic (Debye 1929) and kinetic (Frenkel 1946) models. A modification for these models was made by Fröhlich (1958) and Davidson et Cole (1951). The most recognised equations for dielectric relaxation are the Cole–Cole (Cole, Cole 1941), the Havriliak–Negami (Havriliak, Negami 1967) and the Fuoss–Kirkwood (Fuoss, Kirkwood 1941) equations.

Viscous polymer systems differ both from the Cole–Cole and from the Fuoss–Kirkwood models, so modifications have to be made to them.

It should be noted that two relaxation methods—dielectric spectroscopy and nuclear magnetic relaxation (NMR relaxation)—are widely used for studying molecular order and mobility in polymer systems. For example, both of them are used in (Borisova et al. 1980). However, due to the specific organisation of scientific experiments, the present research is based on the NMR relaxation as the majority of results relevant to this paper were obtained by this method.

Nuclear magnetic relaxation

The majority of studies on relaxation processes in dielectric melts were carried out by NMR relaxation methods. Theoretical background developed by Bloembergen, Purcell, and Pound (Bloembergen et al. 1948) describes relaxation phenomena caused by dipole-dipole interactions of atomic nuclei. The system of nuclear spins forms a thermodynamic spin subsystem. The local magnetic field of this subsystem is sensitive to atomic environment. It can be studied by external alternating magnetic field.

Nuclear magnetic relaxation study: Oligoetheracrilates

NMR relaxation is widely used for studying various polymers and polymer systems (Besghini et al. 2019), such as polystyrene (Gasilova et al. 1993), micellar and liquid crystalline systems (Wong 2006), polyhydroxyalkanoates (Nishida et al. 2018), polyfluoroacryhlates (Borisova et al. 1980) and especially tetrafunctional oligoetheracrilates (OEA) (Fig. 1). The characteristic OEA feature is the formation of insoluble three-dimensional oligomers at early stages of their polymerisation. To explain this phenomenon, Gvozdetskii, Azizov, Gorbunova et al. (Gvozdetskii et al. 1968) suggested that molecules in liquid monomer and polymer systems with acrylic end-groups are set in ordered kinetically preferred states. Those states (LP) were essentially studied by Berlin's group.

Several (from 3 to 5) relaxation areas are characteristic of molecular mobility processes: α, β, and γ transitions (in some cases additional β′, γ′ relaxations are present) (Berlin et al. 1983). Local relaxation processes related to small-scale movements of side groups and main network chains are referred to as β and γ transitions. They occur at lower temperatures, typically 140–180 K.

β′–type relaxation is observed due to freezing of mobility in complex oligomeric chains; for instance, in oligomeric chains containing complex ether groups. Rotational isomerism and rotational vibrations are sometimes believed to be primarily responsible for this type of relaxation.

Additional γ′ relaxation is observed in the case of side methane groups are present in some OEAs, e.g. oligocarbonmethacrylate. Rotation of these groups occurs at higher temperatures.

Processes of a relatively larger scale involve the motion of molecular chain parts with side groups and side chains; oligomers attached to them are known as α relaxation, glass transition being an example (230–360 K).

In three-dimensional (spatially linked) polymers, relaxation processes tend to unite and become non-recognisable (Berlin et al. 1966), which, in turn, can be a sign of a complicated self-assembling process through an intermediate LP stage. Formation of lamellae, globules, and other morphological species suggests the influence of long-range interactions on their creation. Indeed, in α, ω - bis / methacryloiloxy ethyleneoxy carbonyloxy/-1,3-propylene (MEKP) (R= —$(CH_2$—CH_2—$CH_2)$—) the average size of globules was 1 μm (Table 1), which exceeded the definition of "nano". In three-dimensional polymers, such as phenol formaldehyde (Spurr et al. 1957) and epoxy resins (Basin et al. 1972; Erath, Spurr 1959), polymaleinates (Spurr et al. 1957) existence of non-uniform morphology was shown at microscopic scale. For example, for α and γ MEKE (R= —$(CH_2$—$CH_2)$— (α, γ - bis / methacryloiloxy ethyleneoxy carbonyloxy/-1,3-ethylene) aggregation of primary globules followed by the formation

of anizodiametric structures with a characteristic size of 600–800 Å was observed, which was confirmed by SEM and SAX data.
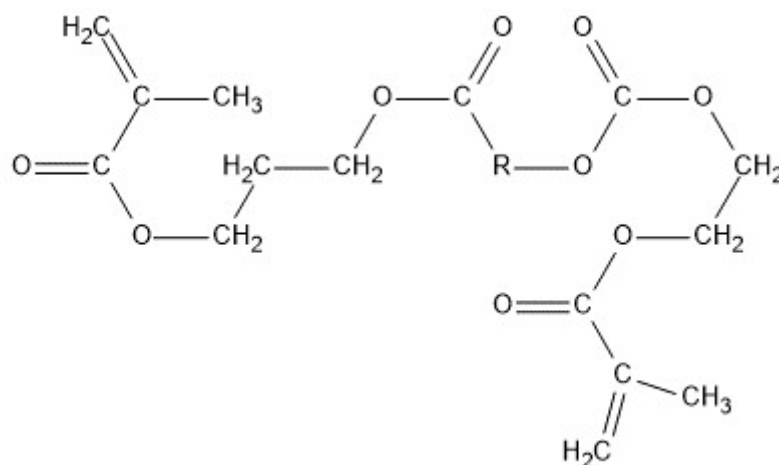
Fig. 1. Tetrafunctional oligoetheracrylates

Supramolecular structure arising during polymerisation in complex polymers (terminology as cited in the original) was discussed by Berlin, Kireeva and Sivergin (1974). Their research concluded that the supramolecular organisation of polymers with highly ordered links of concentration higher than $5 \cdot 10^{20}$ cm^{-3} attained non-uniform, globular structure. The examples of such polymers are phenol-formaldehyde and epoxy resins, polymaleinates, diallyl terephthalates.

Other researchers (Berlin 1970; Berlin et al. 1974; Berlin et al. 1983) came to the same conclusions, stating that the formation of stacked and liquid-crystalline structures was possible in the case of alternating chemically active groups in the structurally regular liquid OAE oligomers. The stability of supramolecular structures was defined by the time of structural relaxation, which, in turn, depends on molecular spatial packing density, magnitude of intermolecular relaxation, viscosity, external conditions, dimensions of pre-cursor oligomers, and polymerisation conditions. Polymerisation conditions stand for the comprehensive influence of operating parameters (vibration, stirring, electromagnetic fields), physical conditions (temperature and pressure), as well as purity and homogeneity of oligomer mixture and other wide range of factors influencing the supramolecular polymer structure. Self-organisation with LP participation is believed to be of interest both for academic and applied science.

In polymers below T_c the scale of pre-pregs containing micelles in sterically preferable positions by the order of magnitude can become close to micelles, distinguishable by electronic microscopy.

Table 1. Average globule size for some OEAs

R	Title	Acronym	Globules size, A
R1	methacryloiloxy ethyleneoxy carbonyloxy/-1,3-ethylene	MEKE	600–800
R2	methacryloiloxy ethyleneoxy carbonyloxy/-1,3-propylene	MEKP	200–1000
R3	methacryloiloxy ethyleneoxy carbonyloxy/-1,3-dimethyl propylene	MEKNPG	1000–1500

Above T_c relaxation studies revealed the existence of complex two-componental absorption lines in OAE, which are defined by Strzlecki, Liebert (1973) as a "molecular collective" formed by Van der Vaals (for non-polar) and dipole-dipole (for polar) molecules. Moreover, it was revealed that molecules in LP exist in the condition of continuous movement and re-organisation, in contrast to relatively stable lamellae above T_c. However, it is not surprising, considering lowered steric limitations at temperatures $T \geq T_c$, but close to T_c, exactly up to $T_c + 40°$. Above the established upper limit, the lifetime of molecular associates became exclusively small ($<10^{-4}-10^{-5}$ s).

In the course of conducted experiments various polymer structures were obtained electrochemically. Electrochemical deposition of conducting polymers onto metal surfaces was performed primarily for the purpose of corrosion protection (Iroh et al. 2003). Examples of morphologies, obtained electro-

chemically, are shown in (Fig. 2) (Levine et al. 2005; 2019). Different electrolyte composition and formation surface resulted in dendritic (Fig. 2A) and vase-looking (Fig. 2B, C) morphologies, which possibly involved air bubbles driven by buoyant force. A structure typical to polypyrrole cauliflower (Fig. 2D) served as a surface for the formation of inverse bell (Fig. 2E), bell (Fig. 2F) and egg-looking (Fig. 2G) morphologies; morphologies obtained by others researches, demonstrated similar bell-shape PPy structures (Ammam 2012), and rectangular patterns (Sapurina, Shishov 2012).
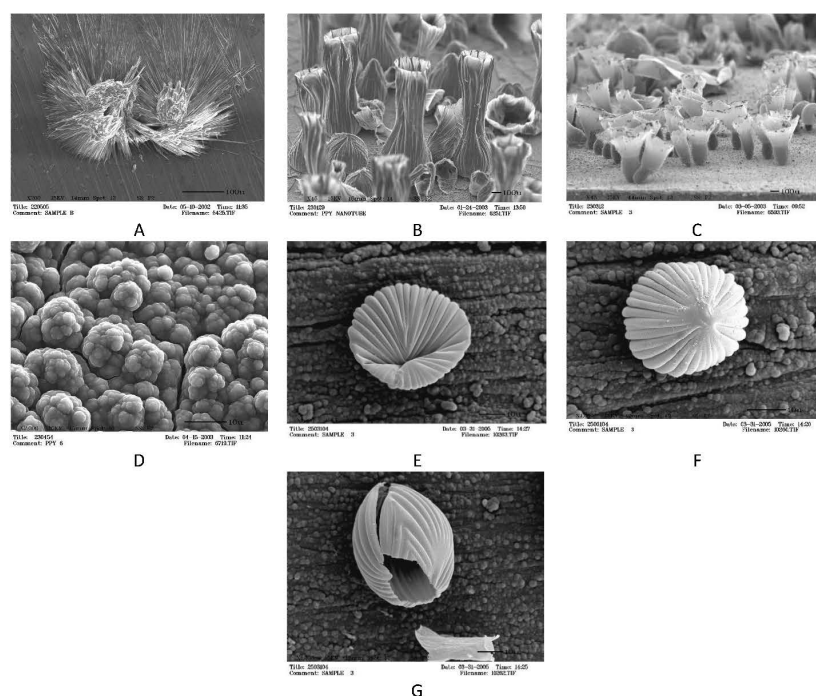
Fig. 2. Morphologies obtained electrochemically

Conclusion

Self-assembling occurs in the process of chemical and electrochemical polymerisation of polymers. As a result, complicated morphologies are formed according to the bottom-up approach. These morphologies belong to both nano and micro-scales. Examples of these morphologies are globules, micelles, lamellae, folds, and microcontainers. Relaxation methods, in particular, nuclear magnetic relaxation and dielectric spectroscopy are sensitive to general parameters related to self-assembling, being together with microscopic methods, a way of its visualization.

References

Ammam, M. (2012) Electrophoretic deposition under modulated electric fields: A review. *RSC Advances*, 2 (20), 7633–7646. DOI: 10.1039/C2RA01342H (In English)

Basin, V. E., Korsunskii, L. M., Shokal'skaya, O. Yu., Aleksandrov, N. V. (1972) O korrelyatsii stabil'nosti nadmolekulyarnoj struktury epoksidnykh smol s ikh elektrofizicheskimi svojstvami [Correlation of the supermolecular structure stability of epoxy resins with their electrophysical properties]. *Vysokomolekulyarnye soedineniya. Seriya A — Polymer Science. Series A*, 14 (9), 2085–2089. (In Russian)

Berlin, A. A., Korolev, G. V., Kefeli, T. Ya., Sivergin, Yu. M. (1983) *Akrilovye oligomery i materialy na ikh osnove [Acrylic oligomers and materials based on them]*. Moscow: Khimiya Publ., 232 p. (In Russian)

Berlin, A. A. (1970) Vliyanie nadmolekulyarnykh obrazovanij v zhidkikh oligomerakh na kinetiku ikh polimerizatsii i svojstva obrazuyushchikhsya vysokopolimerov [Supermolecular aggregates in liquid oligomers and their effect of kinetics of polymerization and properties of the high polymers]. *Vysokomolekulyarnye soedineniya. Seriya A — Polymer Science. Series A*, 12 (10), 2313–2325. (In Russian)

Berlin, A. A., Kireeva, S. M., Sivergin, Yu. M. (1974) *O morfologii, relaksacionnykh i predel'nykh mehanicheskikh svojstvakh trehmernykh polimerov oligoefirakrilatov [On the morphology, relaxation and limiting mechanical properties of three-dimensional polymers of oligoester acrylates].* Dep. to VINITI AN SSSR, 1650–1674, 161. (In Russian)

Berlin, A. A., Tvorogov, N. N., Korolev, G. V. (1966) O fotopolimerizatsii dimetakrilovykh efirov glikolej [About photopolymerization of dimethacrylic esters of glycols]. *Izvestiya Akademii Nauk SSSR. Khimicheskaya seriya — Bulletin of the Academy of Science of the USSR. Chemical Series*, 1, 193–199. (In Russian)

Besghini, D., Mauri, M., Simonutti, R. (2019) Time domain NMR in polymer science: From the laboratory to the industry. *Applied Sciences*, 9 (9), article 1801. DOI: 10.3390/app9091801 (In English)

Bloembergen, N., Purcell, E. M., Pound, R. V. (1948) Relaxation effects in nuclear magnetic resonance absorption. *Physical Review*, 73 (7), 679–715. DOI: 10.1103/PhysRev.73.679 (In English)

Borisova, T. I., Budovskaya, L. D., Ivanova, V. N., Nikonorova, N. A., Rostovskii, Ye. N., Chichagova, Ye. R., Shevelev, V. A. (1980) Issledovanie molekulyarnogo dvizheniya v grebneobraznykh poliftoralkilakrilatakh i metakrilatakh metodami dielektricheskoj i yadernoj magnitnoj relaksatsii [The study of molecular motion in comblike polyfluoroalkylacrylates and methacrylates using dielectric and nuclear magnetic relaxation technique]. *Vysokomolekulyarnye soedineniya. Seriya A — Polymer Science. Series A*, 22 (12), 2672–2681. (In Russian)

Cole, K. S., Cole, R. H. (1941) Dispersion and absorption in dielectrics I. Alternating current characteristics. *The Journal of Chemical Physics*, 9 (4), 341–351. DOI: 10.1063/1.1750960 (In English)

Davidson, D. W., Cole, R. H. (1951) Dielectric relaxation in glycerol, propylene glycol, and *n*-propanol. *The Journal of Chemical Physics*, 19 (12), 1484–1490. DOI: 10.1063/1.1748105 (In English)

Debye, P. J. W. (1929) *Polar molecules.* New York: The Chemical Catalog Company, Inc., 172 p. DOI: 10.1002/jctb.5000484320 (In English)

Erath, E. H., Spurr, R. A. (1959) Occurrence of globular formations in thermosetting resins. *Journal of Polymer Science*, 35 (129), 391–399. DOI: 10.1002/pol.1959.1203512907 (In English)

Faynman, R. P. (1960) There's plenty of room at the bottom. *Engineering and Science*, 23 (5), 22–36. (In English)

Frenkel, J. (1946) *Kinetic theory of liquids.* Oxford: Oxford University Press, 485 p. (In English)

Fröhlich, H. (1958) *Theory of dielectrics: Dielectric constant and dielectric loss.* 2nd ed. Oxford: Clarendon Press, 192 p. (In English)

Fuoss, R. M., Kirkwood, J. G. (1941) Electrical properties of solids. VIII. Dipole moments in polyvinyl chloride-diphenyl systems. *Journal of the American Chemical Society*, 63 (2), 385–394. DOI: 10.1021/ja01847a013 (In English)

Gasilova, E. R., Shevelev, V. A., Ginzburg, L. I., Tarkova, E. M. (1993) Issledovanie fazovogo sostava i stepeni sshivaniya dispersnoj uprochnyayushchej fazy udaroprochnogo polistirola s pomoshch'yu protonnoj magnitnoj relaksatsii [Study of phase composition and crosslinking in dispersed strengthening phase of high impact strength polystyrene by ^{1}H magnetic relaxation]. *Vysokomolekulyarnye soedineniya. Seriya A — Polymer Science. Series A*, 35 (3), 280–284. (In Russian)

Gvozdetskii, A. N., Azizov, A. G., Gorbunova, N. V., Kabanov, V. A. (1968) O roli labil'nykh zagotovok pri sopolimerizatsii akrilonitrila s metilmetakrilatom pri temperaturnykh fazovykh perekhodov steklo—kristall [About role of mobile organized molecular arrays at copolymerization of acrylonitrile with methylmethacrylate at temperatures of phase transitions glass—crystall]. *Vysokomolekulyarnye soedineniya. Seriya A — Polymer Science. Series A*, 10 (8), 1817–1822. (In Russian)

Havriliak, S., Negami, S. (1967) A complex plane representation of dielectric and mechanical relaxation processes in some polymers. *Polymer*, 8, 161–210. DOI: 10.1016/0032-3861(67)90021-3 (In English)

Iroh, J. O., Zhu, Y., Shah, K. et al. (2003) Electrochemical synthesis: A novel technique for processing multi-functional coatings. *Progress in Organic Coatings*, 47 (3–4), 365–375. DOI: 10.1016/j.porgcoat.2003.07.006 (In English)

Lehn, J.-M. (1988) Supramolecular chemistry — scope and perspectives. Molecules, supermolecules, and molecular devices (Nobel Lecture). *Angewandte Chemie, International Edition*, 27 (1), 89–112. DOI: 10.1002/anie.198800891 (In English)

Levine, K. L., Guolian, Ch., He, J. et al. (2015) Unusual Polypyrrole structures observed during electrodeposition of Polypyrrole. In: *CPM poster session*: *NDSU-2015. August 2015. Conference Proceedings*. NDSU, Fargo ND, USA. (In English)

Levine, K. L., Nikonorova N. A., Khanin S. D. (2019) Protsessy samoorganizatsii pri polimerizatsii i elektropolimerizatsii v polimernykh sistemakh [Self-organisation processes under polymerization and electropolymerizing in polymer systems]. In: *XIII St. Petersburg congress "Professional education, science and innovations in XXI century". 20–22 November, 2019. Conference Proceedings*. Saint Petersburg: Saint Petersburg Mining University Publ., 128–131. (In Russian)

Nicolis, G., Prigogine, I. (1977) Part IV. Control mechanisms in chemical and biologycal systems. In: G. Nicolis, I. Prigogine. *Self-organization in nonequilibrium systems: From dissipative structures to order through fluctuations*. New York: Wiley InterScience, 339–426. (In English)

Nishida, M., Tanaka, T., Hayakawa, Y., Nishida, M. (2018) Solid-state nuclear magnetic resonance (NMR) and nuclear magnetic relaxation time analyses of molecular mobility and compatibility of plasticized polyhydroxyalkanoates (PHA) copolymers. *Polymers*, 10 (5), article 506. DOI: 10.3390/polym10050506 (In English)

Sapurina, I. Yu., Shishov, M. A. (2012) Oxidative polymerization of aniline: Molecular synthesis of polyaniline and the formation of supramolecular structures. In: A. de Souza Gomes (ed.). *New polymers for special applications.* Croatia: IntechOpen Publ., 251–312. DOI: 10.5772/48758 (In English)

Spurr, R. A., Erath, E. H., Myers, H., Pease, D. C. (1957) Curing process in phenolic resins electron-microscopic analysis. *Industrial & Engineering Chemistry*, 49 (11), 1839–1842. DOI: 10.1021/ie50575a027 (In English)

Strzelecki, I., Liebert, L. (1973) Sur la synthèse de quelques nouveaux monomères mesomorphes. Polymérization de la p-acryloyloxybenzylidene p-carboxyaniline. *Bulletin de la Société Chimique de France*, 2, 603–604. (In French)

Wong, T. C. (2006) Micellar systems: Nuclear magnetic resonance spectroscopy. In: N. Somasundaran (ed.). *Encyclopedia of surface and colloid science. Vol. 5.* 2nd ed. New York: Taylor & Francis, 3738–3756. (In English).

Influence of particle aspect ratio and ability to aggregate on electrical conductivity of fiber-forming polymer composites

E. S. Tsobkallo✉1, O. A. Moskalyuk1, V. E. Yudin2, A. N. Aleshin3

1 Saint-Petersburg State University of Industrial Technologies and Design,
18 Bolshaya Morskaya Str., Saint Petersburg 191186, Russia
2 Institute of Macromolecular Compounds of Russian Academy of Sciences,
31 Bolshoy Ave., Saint Petersburg 199004, Russia
3 Ioffe Institute, 26 Politekhnicheskaya Str., Saint Petersburg 194021, Russia

Authors

Ekaterina S. Tsobkallo, e-mail: tsobkallo@mail.ru

Olga A. Moskalyuk

Vladimir E. Yudin, ORCID: 0000-0002-5517-4767

Andrey N. Aleshin

Abstract. Fiber-forming polymer composites filled with carbon nanoparticles of three types (carbon black is a spherical filler; carbon nanofibers and carbon nanotubes are anisotropic nanoparticles) were produced by melt technology. Electrical conductivity of the fiber-forming polymer composites was measured; a function of the filler concentration and the percolation thresholds were determined. It was found that an increase in the aspect ratio of carbon nanoparticles leads to a decrease in the percolation threshold. The correlation between the axial ratio, stiffness, filler concentration and electrical conductivity of the percolation cluster in fiber-forming polymer composites was analysed.

Keywords: polymer composites, carbon particles, fiber-forming, electrical conductivity, percolation threshold, aspect ratio, aggregate.

Introduction

In recent decades electrically conductive composite materials based on polymer matrices have been in the spotlight of a range of technological fields from aircraft and tool engineering to medicine. The interest arises from the fact that electrical characteristics of such composites are close to the properties of metals, whereas mechanical properties and processing methods are typical for plastics.

The special properties of composites depend on filler concentration of nanoparticles and the shape of filler particles dispersed in the polymer matrix. The latter characteristic for nanocomposite materials is usually difficult to assess. For this reason, it is important to attempt establishing a correlation between the particle aspect ratio, ability to aggregate, and electrical conductivity of the composite material, which can be measured using simple methods. The presence of aggregates in the polymer matrix leads to a decrease in mechanical characteristics of electrically conductive polymer composites. Therefore, it is the electrical conductivity values of the composite material that make it possible to evaluate the quality of the technology used to introduce electrically conductive nanoparticles into the polymer and the dispersion degree of the filler. Polymer composites filled with dispersed carbon particles (especially carbon

nanotubes) are of special interest to both theoretical and applied science because the use of carbon nanotubes allows changing electrical conductivity in a wide range of values and improving mechanical characteristics of polymer matrices (Kymakis et al. 2002; Moskalyuk et al. 2012; Tarfaoui et al. 2017).

The percolation theory formulated for a continuous medium is often used to describe electrical properties of a composite material filled with electrically conductive particles (Fig. 1). According to this theory, each point of the space corresponds to electrical conductivity $\sigma = \sigma_f$ with the probability $p = \vartheta_f$ and to electrical conductivity $\sigma = \sigma_m$ with the probability $1 - p$. Here, ϑ_f is the fraction of conducting particles in the bulk of the polymer matrix; σ is electrical conductivity; and the indices *f* and *m* denote the filler and the matrix, respectively (Kinloch et al. 2018; Moskalyuk et al. 2012; Tarfaoui et al. 2017).
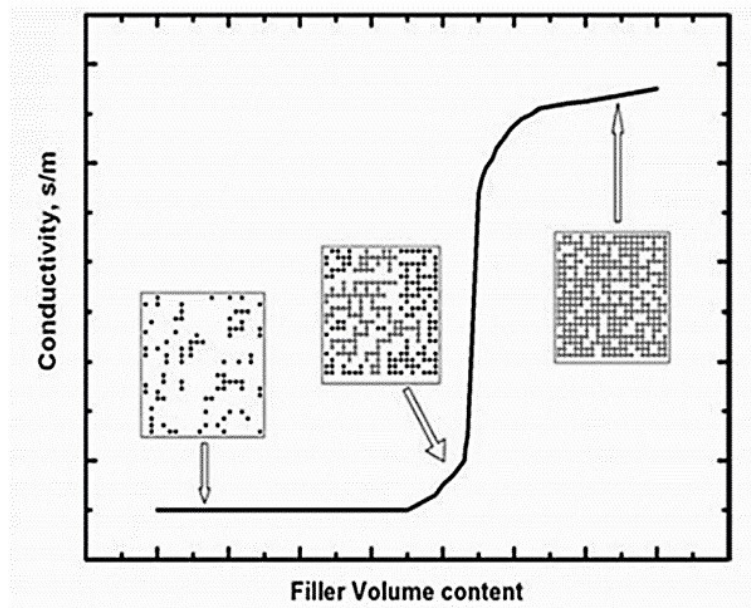
Fig. 1. Dependence of the polymer composites conductivity on the filler content

The percolation threshold in this case is equal to the minimum fraction of the space occupied by conducting regions at which the system is still conducting (Kinloch et al. 2018). Electrical conductivity of the composite material increases non-monotonically: the most dramatic change in electrical conductivity occurs, as a rule, in a narrow range of filler concentrations, which suggests a dielectric–metal transition or a percolation transition when the quantity ϑ_f is equal to the percolation threshold (Kinloch et al. 2018; Moskalyuk et al. 2012). At filler concentrations above and below the percolation threshold, dependence of the composite material electrical conductivity on the concentration of the carbon filler differs significantly. At low concentrations of the filler (the first horizontal section in Fig. 1), all conductive particles introduced into the polymer matrix are combined into finite-size clusters that are isolated from each other. With increasing concentration of conductive particles, the average cluster size also increases. At $\vartheta_f = \vartheta_f^*$, most of the clusters at first isolated from each other are combined into an infinite cluster, penetrating the entire system with the formation of a conduction channel (Kinloch et al. 2018; Matos et al. 2019; Moskalyuk et al. 2012). With the further increase in the concentration of the conducting filler, the volume of the endless cluster increases as a result of absorption of the final clusters, especially the largest ones. Thus, the average size of the final clusters decreases (Kinloch et al. 2018; Matos et al. 2019; Moskalyuk et al. 2012).

The description of the correlation between physical and geometric analyses is the main task of percolation theory. One of the simplest approaches and, consequently, the most studied one is the description of structures based on regular lattices. In this approach, the identification of nodes and links that have a certain fraction (1-p) of randomly selected nodes (along with outgoing links) or a part of randomly selected links is performed. The answer (cut) is determined in such a way that the grid breaks into two parts. During the node identification, nodes are blocked (network nodes are destroyed) (Matos et al. 2019). Percolation on a square grid is just one of possible patterns. It is also possible to study percolation on triangular and hexagonal grids, trees, as well as on more complex (three-dimensional) lattices,

for example, cubic ones. The grid does not have to be regular. Random lattice processes are also considered (Kovacs et al. 2007).

<div align="center">(a)   (b)</div>
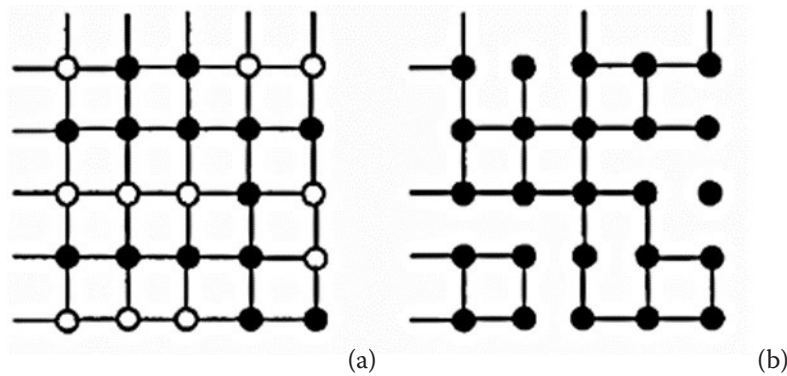
Fig. 2. The knot problem (a) and the connection problem (b) on a square lattice

The analysis of the topology of an infinite cluster showed that it contributes to infinite clustering and permittivity, but not to conductivity (Kovacs et al. 2007; Matos et al. 2019). Such chains were called "dead ends". An infinite cluster without dead ends was called a skeleton of an infinite cluster. A skeleton of an infinite cluster was first described in the Shklovskii–De Gennes model (Efros, Shklovskii 1976; Li et al. 2006; Ukshe et al. 2020). It is an irregular lattice with an average distance between nodes, depending on the proximity of the filler concentration to the percolation threshold.

$$\sigma_c = \sigma_f \, (\vartheta_f - \vartheta_f^*)^\beta, \text{ if } \vartheta_f > \vartheta_f^*$$
$$\sigma_c = \sigma_f \, (\vartheta_f - \vartheta_f^*)^\beta, \text{ if } \vartheta_f < \vartheta_f^*$$
$$\sigma_c \approx \sigma_f X^\delta, \text{ if } \vartheta_f \approx \vartheta_f^*,$$

where $X = \sigma_2/\sigma_1 \ll 1$; Table 1 provides the parameters α, β, and $\delta = \beta / (\alpha + \beta)$ for different flow models.

Table 1. Parameters of some percolation models near the percolation threshold

	Cn	α	β	δ
Three-dimensional connection problem (cubic lattice)	0.25	1	1.6	0.67
Two-dimensional connection problem (square lattice)	0.5	1	1.1	0.51
Three-dimensional flow model (continuous medium)	0.145	1	1.4	0.65

In the case of a polymer composite filled with anisotropic electrically conductive fillers (e. g., carbon nanotubes), the conductive cluster may consist of randomly oriented anisometric particles (fibers, cylinders). Electrical conductivity of such a polymer composite is always anisotropic (Kinloch et al. 2018; Kymakis et al. 2002; Moskalyuk et al. 2012; Tarfaoui et al. 2017). Polymer composites filled with anisotropic fillers usually have a considerably lower percolation threshold than polymer composites filled with spherical or spheroidal particles. Electrical properties of composite materials with anisotropic spheres or isotropic elongated particles were previously investigated in detail (Kinloch et al. 2018; Kymakis et al. 2002; Moskalyuk et al. 2012; Tarfaoui et al. 2017).

The aim of this study was to investigate electrical conductivity of fiber-forming polymer composites filled with two types of carbon nanoparticles: spherical particles with an aspect ratio 1—carbon black—and particles with a high aspect ratio—carbon nanofibres and carbon nanotubes—in which the L/D is 10 times different from each other. Nanoparticles used in the study vary in size, shape (aspect ratio) and hardness. Hardness of the filler is crucial for the effective introduction of nanoparticles into the fiber-forming polymer matrix and ensuring high conductivity because only hard particles are able to maintain their original shape when introduced into the polymer matrix (Kinloch et al. 2018; Moskalyuk et al. 2012; Tarfaoui et al. 2017). For example, this property is observed in such carbon particles as carbon black and carbon nanofibers which have the necessary rigidity. Unlike them, such flexible structures as

carbon nanotubes, which have the highest aspect ratio of all carbon particles, can retain their original shape in the bulk of the polymer matrix or may lose it. If carbon nanotubes take the form of globules, spirals or aggregates, the optimal values of electrical conductivity in the polymer composite cannot be achieved, and this can also lead to a deterioration in mechanical properties (Kymakis et al. 2002; Moskalyuk et al. 2012). An attempt was made to relate the shape of the carbon nanoparticles dispersed in the fiber-forming polymer to the threshold concentration of the percolation cluster formation and electrical conductivity of a percolation cluster at the percolation threshold.

The aim of this study was to obtain fiber-forming polymer composite based on polypropylene matrix filled with different types of carbon particles using melt technology and investigate the influence of particle aspect ratio and ability to aggregate on electrical conductivity of composites.

Sample preparation and experiment

The fiber-forming polymer matrix was isotactic polypropylene Balen 01270 (Ufa Petroleum Refinery, Bashneftekhim, Ufa). The density was 0.9 g/cm^3; melt flow rate (MFR) was 27–30 g/10 min.

Carbon black (CB) P-805 E, graphitised carbon nanofibers (CNF) VGCF-H by Showa Denko K. K., Japan, and multi-walled carbon nanotubes (CNT) CTube-100 by CNT Co., LTD, Korea, were used as fillers for fiber-forming polymer composites. The parameters of the carbon nanoparticles used are presented in Table 2.

Table 2. Parameters of the carbon fillers used

Characteristic	Carbon black P-805 E	Carbon nanofibers VGCF	Multi-walled carbon nanotubes CTube-100
Aspect ratio (L/D ratio)	~1	~30	~400
Electrical resistivity, S/m	10^{-1}	10^{-2}	$10^{-5}-10^{-1}$

Carbon black is a cluster consisting of primary particles with an average size of ~80 nm and has an almost spherical or ellipsoidal shape with an aspect ratio of order unity. Carbon nanofibers have the form of rigid cylinders from 100 to 150 nm in diameter, which are characterised by a moderate aspect ratio of ~30. Carbon nanotubes are flexible fibers from ~10 to ~40 nm in diameter with a very large axial ratio average ~400.

The samples of fiber-forming polymer composites were prepared using melt blending technology with a DSM Xplore 5 ml Twin Screw Microcompounder (Netherlands). Dispersion of the filler in the polymer melt was carried out for 5 minutes at a temperature of 200°C and a screw rotation speed of 75 rpm. Then the fiber was extruded through a round die installed at the exit of the Twin Screw Microcompounder chamber. Immediately after leaving the spinneret, the fiber-forming polymer material was rapidly cooled and wound at a constant speed on coils of the receiver device. Composite fibers had a diameter of 400 μm.

The current–voltage characteristics of the fibers were measured at a direct current in the voltage range from −100 to +100 V using an automated setup based on a Keithley 6487 picoammeter and an AKIP_1124 programmable power supply.

The dispersion quality of nanoparticles in the bulk of the polypropylene matrix was controlled by examining the fracture surfaces of the samples of the composite fibers with a Supra 55 scanning electron microscope (Carl Zeiss, Germany). In order to remove the charge of static electricity and to improve the contrast, gold was evaporated onto the surface under investigation.

Results and discussion

The change in electrical conductivity of the fiber-forming polymer composites according to the filler concentration with different morphologies and sizes (CB, CNF, CNT) is presented in Fig. 3. Pure polypropylene has electrical conductivity of ~10^{-14} S/m.
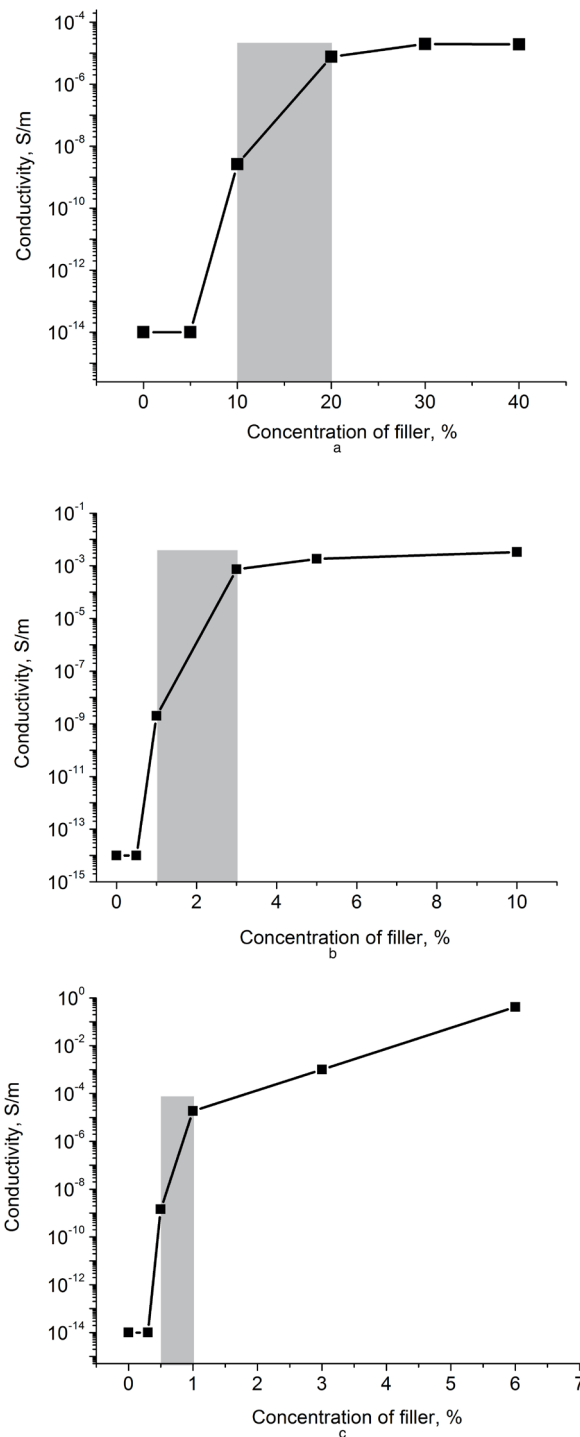
Fig. 3. Change in electrical conductivity of composite materials based on polypropylene according
to the concentration of (a) carbon black, (b) graphitised carbon nanofibers, (c) multi-walled carbon nanotubes.
The percolation threshold is highlighted in colour

Fig. 3 shows three clearly distinguishable sections in the concentration dependences of electrical conductivity for all fiber-forming polymer composite materials: the first one is a horizontal section where the filler concentration is not sufficient to form an electrically conductive cluster in the volume of the polymer matrix; the second one is a steep section with a sharp increase in electrical conductivity with an increase in filler concentration, i.e. a conducting cluster is formed; and the third section is the smoothed part of the increase in electrical conductivity with an increase in filler concentration above the percolation threshold. Cryo-cleavage micrographs of fiber-forming polymer composite fibers are presented in Fig. 4.
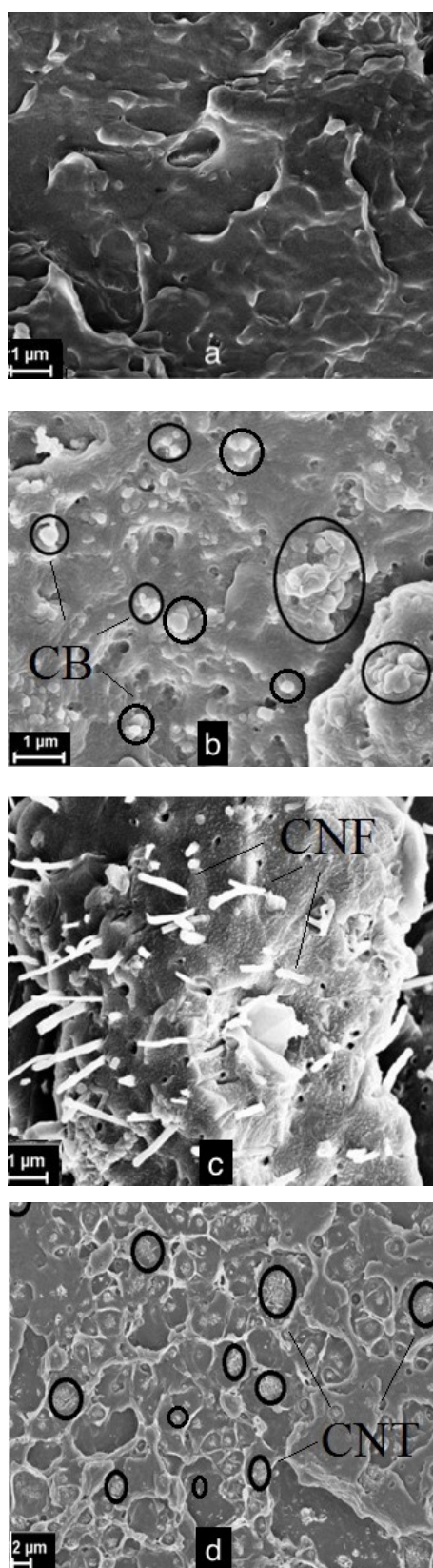
Fig. 4. Cleavage micrographs of (a) pure polypropylene fibers and (b) polypropylene filled with 20% carbon black, (c) 10% graphitised carbon nanofibers and (d) 6% multi-walled carbon nanotubes

As can be seen from Fig. 4b, carbon black is dispersed in a fiber-forming polypropylene matrix both at the size of the primary particles and with the formation of conglomerates up to 2 microns in size. With an increase in the filler concentration, conglomerate sizes also increase. Carbon nanofibers up to the

maximum filling, dispersible in a fiber-forming polypropylen composites, retain their original shape (Fig. 4c). At the same time more flexible carbon particles (carbon nanotubes) with a high aspect ratio demonstrate the ability to aggregate (Fig. 4d). The average aggregate size is 2 microns.

Summarising the above results, the filler concentration and shape of the percolation cluster for the fiber-forming composite fibers are listed in Table 3. The nanoparticle concentration at the percolation cluster was determined in the middle of the increasing straight-line section.

Table 3. Filler concentration and shape of the percolation cluster for the fiber-forming composite fibers

Reference parameter	CB	CNF	CNT
Filler concentration of the percolation cluster, wt%	15	2	0.75
Piece shape of the percolation cluster			

Based on the $\sigma(\vartheta)$ dependence, percolation thresholds are established for fiber-forming polymers filled with carbon nanoparticles with a typical axial ratio: 10–20 wt% for CB, 1–3 wt% for CNF and 0.5–1.0 wt% for CNT (Fig. 3, the percolation threshold is highlighted in colour). In the case of carbon black (particles with L/D ratio~1), the conductive cluster is a chain of their conglomerates. For CNF (hard particles with L/D~30), a conducting cluster is formed due to contacts between individual particles. For CNT (flexible particles with a high aspect ratio L/D~400), a conducting cluster is formed of single particles and their aggregates.

The nanoparticle concentrations determined at the percolation threshold and after the percolation threshold at the maximum concentration of carbon nanofillers are listed in Table 4. Electrical conductivity at the percolation cluster was determined in the middle of the increasing straight-line section.

Table 4. Electrical conductivity of the fiber-forming composite fibers

Reference parameter	CB	CNF	CNT
Electrical conductivity of the percolation cluster, S/m	$\sim 10^{-7}$	$\sim 10^{-6}$	$\sim 10^{-6}$
Electrical conductivity at the maximum concentration of carbon nanofillers, S/m	$\sim 10^{-4}$	$\sim 10^{-3}$	$\sim 10^{0}$

In the case of fiber-forming composites filled with spherical carbon particles, electrical conductivity of the percolation cluster is $\sim 10^{-7}$ S/m; for composites filled with anisotropic particles (CNF and CNT), electrical conductivity of the percolation cluster is an order of magnitude higher. Thus, an increase in the axial ratio of CNT in comparison with CNF does not lead to an increase in electrical conductivity of the percolation cluster. For carbon black particles with L/D~1 electrical conductivity at the maximum filler concentration is $\sim 10^{-4}$ S/m. With aspect ratio increased by thirty times (CNF) electrical conductivity at the maximum filler concentration is $\sim 10^{-3}$ S/m. For carbon particles L/D~400 (CNT) electrical conductivity at the maximum filler concentration is $\sim 10^{0}$ S/m.

The following conclusions can be drawn from the data presented in Fig. 3 and in Tables 3 and 4. An increase in the aspect ratio of nanoparticles leads to a decrease in the threshold concentration of the filler and electrical conductivity of the percolation cluster increases by an order of magnitude. Thus, the effect is observed when comparing the results obtained for fiber-forming polymer composites filled with carbon black and carbon nanofibers, the aspect ratio of which is 30 times different (Kinloch et al. 2018; Moskalyuk et al. 2012; Tarfaoui et al. 2017). An increase in the concentration of CB and CNF above the percolation threshold does not any further lead to an increase in electrical conductivity of fiber-forming composites. This effect means that the contribution to electrical conductivity from the conducting

clusters formed upon the introduction of additional carbon particles above the percolation threshold is significantly less than conductivity of the polymer composite formed during the formation of the percolation threshold (Kinloch et al. 2018; Moskalyuk et al. 2012).

Comparison of the data obtained for fiber-forming polymer composites filled with CNF and CNT has demonstrated that an increase in the aspect ratio of carbon nanoparticles by 10 times decreases the percolation threshold. It should be noted that the percolation threshold in composites filled with carbon nanotubes is usually lower than the values obtained in this study. Since the CNT conductivity is at or lower than that of CNF (Table 2) and the aspect ratio is 10 times greater than that of CNF, we can conclude that flexible carbon particles (nanotubes) do not retain an elongated, almost straight shape when dispersed into a fiber-forming polymer matrix, which does not allow to obtain an effective increase in electrical conductivity of the polymer (Fig. 4d). Therefore, the technology used to introduce nanoparticles into a fiber-forming polymer is suitable only for the preparation of a composite with rigid (i.e. not flexible) nanoparticles, such as CB and CNF, while its usage for flexible carbon structures (carbon nanotubes) is not justified. Microphotography shows that carbon nanotubes do not generally retain their straight shape when introduced into a fiber-forming polymer matrix; instead, they form dense clusters and globules. Therefore, the final sizes of electrically conducting particles and their aspect ratio change and differ significantly from the original ones (Kinloch et al. 2018; Moskalyuk et al. 2012; Tarfaoui et al. 2017). Future studies should lead to the development of alternative ways to introduce flexible carbon nanoparticles into a fiber-forming polymer matrix. This will allow us to use such unique particles more efficiently in order to create electrically conductive polymer composites.

Thus, it is impossible to draw conclusions about the effect of electrically conductive fillers on electrical conductivity of the fiber-forming polymer matrix based on their aspect ratios only. It is necessary to confirm that the nanoparticles dispersed in the polymer matrix retain a shape that is close to rectilinear.

Conclusions

Fiber-forming polymer composites filled with carbon nanoparticles with different aspect ratio (carbon black, graphitised carbon nanofibers and multi-walled carbon nanotubes) were obtained in laboratory conditions using a twin-screw microextruder. Electrical conductivity of the fiber-forming polymer composite was measured. The dependence of electrical conductivity of the filler concentration has a threshold character. The percolation thresholds were observed at concentration 10–20 wt% for spherical particles (carbon black), at concentration 1–3 wt% for anisotropic nanoparticles and 0.5–1.0 wt% in the case of carbon nanofibers and carbon nanotubes. The percolation threshold can be shifted towards the lower filler concentrations with an increase in the aspect ratio of electrically conductive nanoparticles. In this case, electrical conductivity of the percolation cluster can increase by one order of magnitude. To use electrically conductive nanoparticles with a high aspect ratio as efficiently as possible when creating fiber-forming polymeric composites, it is necessary to take into account not only the L/D of fillers, but also the nature of their dispersion in the polymer matrix. Flexible nanoparticles with a high aspect ratio should maintain an almost rectilinear shape when dispersed into a polymer matrix.

References

Efros, A. L., Shklovskii, B. I. (1976) Critical behaviour of conductivity and dielectric constant near the metal-non-metal transition threshold. *Physica Status Solidi: Basic Solid State Physics*, 76 (2), 475–485. DOI: 10.1002/pssb.2220760205 (In English)

Kinloch, I. A., Suhr, J., Lou, J., Young, R. J., Ajayan, P. M. (2018) Composites with carbon nanotubes and graphene: An outlook. *Science*, 362 (6414), 547–553. DOI: 10.1126/science.aat7439 (In English)

Kovacs, J. Z., Velagala, B. S., Schulte, K., Bauhofer, W. (2007) Two percolation thresholds in carbon nanotube epoxy composites. *Composites Science and Technology*, 67 (5), 922–928. DOI: 10.1016/j.compscitech.2006.02.037 (In English)

Kymakis, E., Alexandou, I., Amaratunga, G. A. J. (2002) Single-walled carbon nanotube–polymer composites: Electrical, optical and structural investigation. *Synthetic Metals*, 127 (1–3), 59–62. DOI: 10.1016/S0379-6779(01)00592-6 (In English)

Li, Y.-J., Xu, M., Feng, J.-Q., Dang, Z.-M. (2006) Dielectric behavior of a metal-polymer composite with low percolation threshold. *Applied Physics Letters*, 89 (7), article 072902. DOI: 10.1063/1.2337157 (In English)

Matos, M. A. S., Pinho, S. T., Tagarielli, V. L. (2019) Predictions of the electrical conductivity of composites of polymers and carbon nanotubes by an artificial neural network. *Scripta Materialia*, 166, 117–121. DOI: 10.1016/j.scriptamat.2019.03.003 (In English)

Moskalyuk, O. A., Aleshin, A. N., Tsobkallo, E. S., Krestinin, A. V., Yudin, V. E. (2012) Electrical conductivity of polypropylene fibers with dispersed carbon fillers. *Physics of the Solid State*, 54 (10), 2122–2127. DOI: 10.1134/S1063783412100253 (In English)

Tarfaoui, M., El Moumen, A., Lafdi, K. (2017) Progressive damage modeling in carbon fibers/carbon nanotubes reinforced polymer composites. *Composites Part B: Engineering*, 112, 185–195. DOI: 10.1016/j.compositesb.2016.12.056 (In English)

Ukshe, A., Glukhov, A., Dobrovolsky, Y. (2020) Percolation model for conductivity of composites with segregation of small conductive particles on the grain boundaries. *Journal of Materials Science*, 55 (15), 6581–6587. (In English)

Synchrotron radiation photoemission study of Ba adsorption on the vicinal SiC(111)-8° surface

G. V. Benemanskaya[✉1], S. N. Timoshnev[2]

[1] Ioffe Institute, 26 Politekhnicheskaya Str., Saint Petersburg 194021, Russia
[2] Alferov University, 8/3 Khlopina Str., Saint Petersburg 194021, Russia

Authors

Galina V. Benemanskaya, ORCID: 0000-0002-2399-3223, e-mail: galina.benemanskaya@mail.ioffe.ru

Sergei N. Timoshnev, ORCID: 0000-0002-9294-3342

Abstract. The electronic structure of the Ba/SiC(111)-8° interface has been studied in detail in situ in an ultrahigh vacuum using synchrotron radiation photoelectron spectroscopy. The SiC(111)-8° samples were grown by an original method of epitaxy of low-defect unstressed nanoscaled silicon carbide films on silicon substrates. The Si $2p$, C $1s$ core level spectra have been investigated as a function of Ba submonolayer coverage with photon energies in the range of 100–450 eV. Upon Ba adsorption, a drastic change in the C $1s$ spectrum was revealed. It was found that Ba adsorption leads to the formation of a new, previously unknown carbon-based structure of C nanoclusters on the surface. Experimental data show that the nanoclusters can be created exclusively on the vicinal SiC(111)-8° surfaces in the presence of stabilizing adsorbed metal atoms, specifically, Ba atoms. It is shown that the surface nanoclusters are formed due to the local interaction between silicon vacancies, carbon atoms and Ba adatoms. It is established that the carbon clusters are composed of carbon rings and their chemical bonds are similar in nature to the bonds in aromatic-like compounds.

Keywords: silicon carbide, interfaces, surface, nanostructures, photoelectron spectroscopy, electronic structure.

Introduction

The development of a high-quality wide-band gap silicon carbide semiconductor is one of the key issues in micro- and nanoelectronics. Silicon carbide shows promise for electronic devices that can perform under extreme conditions such as high temperature, high voltage, high power and frequency. Besides, SiC is a promising material for biophysics applications (Eddy, Gaskill 2009). The majority of applications are oriented toward thin film geometries. The main obstacle to growing low-defective films on Si is the elastic stress due to the mismatch between the lattice parameters of a semiconductor layer and a silicon substrate. To obtain stress-free SiC films, an original method was proposed for the synthesis of epitaxial layers: the substrate is involved in a chemical reaction and the reaction product grows inside the substrate layer (Kukushkin, Osipov 2013; Kukushkin, Osipov 2014).

It was found that the most advantageous location of the dipoles is the direction (111) in crystals with cubic symmetry. In this condition, the elastic energy is relaxed due to the attraction of point defects formed during the chemical reaction in anisotropic media. The theoretical and experimental evidence for a completely new method of growing defect-free silicon carbide films on silicon substrate was proposed in the review (Kukushkin, Osipov 2014) and references therein. The integration of new-grown SiC

nanolayers into silicon technology requires studies of surface properties, and, in particular, the interface formation.

Surface electronic properties of brand new SiC nanolayers are still poorly understood. This gives rise to a controversy with regard to surface state spectra, interface formation, band-bending, and the effect of 2D phase transition. These surface and interface boundary regions are crucial which is why these data are so valuable. However, the surface, near surface and interface electronic structure of SiC remains unclear and needs further investigation. Alkali-earth metal and alkali metal adsorbates are good candidates for the formation of metal-semiconductor interfaces and Schottky barrier compositions. The relevant electronic properties were studied for Sc/3C-SiC(111) interface (King et al. 2015), Rb and Cs adsorption on graphene on SiC(0001) (Watcharinyanon et al. 2011) and Na on graphene on SiC(0001) (Watcharinyanon et al. 2012). It was found that Rb, Cs and Na deposited on monolayer graphene samples produce an *n*-type doping with the electron transfer from the metal to the graphene layer.

Photoelectron spectroscopy (PES) is an effective tool to study the electronic structure of both the semiconductor bulk and surface. The electronic structure of SiC grown conventionally has been the focus of a number of experimental and theoretical investigations (Virojanadara et al. 2008; Su et al. 2012; Bechstedt, Furthmüller 2004; Wang et al. 2009). Photoelectron spectroscopy was used to study the surface-related properties in the energy range of the valence band (VB). The obtained conditions were reported to be correlated with the Si dangling bonds and the interaction between the Si top atoms and C atoms. This outcome was predicted in the investigations based on the density functional theory within the local density approximation. Moreover, these calculations showed that the surface electronic states below the Fermi level may originate from the Si-dangling bonds of the SiC surface (Abavare et al. 2013). Only a few studies focus on the valence band and Si 2*p*, C 1*s* core level spectra for SiC(111) as well as the vicinal SiC(111)-4° and SiC(111)-8° surfaces (Su et al. 2012; Takahashi et al. 2011; Bosi et al. 2013). Recently, photoelectron spectroscopy was used to study the Ba/SiC(111)-8° and Cs/SiC(111)-8° interfaces. The study revealed significant changes in surface electronic properties (Benemanskaya et al. 2019a; 2019b).

This paper reports the results of the study of the evolution of electronic structure of the Ba/Si(111)-8° interface as a function of Ba coverage. The data were collected using synchrotron-radiation based photoemission spectroscopy.

Materials and methods

Photoemission studies were carried out at BESSY II (Helmholtz Zentrum Berlin) using the synchrotron radiation with photon energies in the range of 100–450 eV. The PES experiments were performed *in situ* in an ultrahigh vacuum of 5×10^{-10} Torr at room temperature. The SiC sample was preliminary heated *in situ* at a temperature of ~900 K. The spectra were measured in normal emission. For the new SiC nanolayer the photoemission spectra of Si 2*p*, C 1*s*, Ba 4*d* core levels were recorded. The main elements presented in the PES overview of the clean SiC surface were Si, C and negligible O. No other elements were detected in significant amounts. A total energy resolution of better than 100 meV was used.

The single-crystal SiC/Si(111)-8° epitaxial layer of the thickness of ~100 nm was grown on vicinal Si(111)-8° substrate using the original method (Kukushkin, Osipov 2013; Kukushkin, Osipov 2014). The structure of the SiC sample was ascertained by angle spectroscopic ellipsometry and electron microscopy. The surface morphology of the sample was characterized by atomic force microscopy. Atomically pure barium was adsorbed onto the SiC/Si(111)-8° surface from a standard source. Step-by-step deposition of Ba coverage was used. Note that the Ba sticking coefficient is equal to one up to 1 monolayer (1 ML). The Ba overlayer corresponding to 1 ML can be estimated from the dependence of the Ba 4*d* core level peak intensity as a function of the Ba deposition time (Okuda et al. 2005). This made it possible to determine the Ba coverage deposited onto the sample to better than 10%. Note that 1 ML is defined as one complete layer of Ba atoms and as equal to $\sim 6.25 \times 10^{14}$ atoms/cm^2.

Results and discussion

Figure 1 represents the C 1*s* core level spectra taken from the clean vicinal SiC(111)-8° surface (Fig. 1, curve 1) and from the Ba/Si(111)-8° interface at different Ba coverages (Fig. 1, curves 2, 3). The C 1*s* core level spectrum for the clean SiC(111)-8° surface is found to be composed of two main peaks B and S1 (Fig. 1, curve 1). One peak B at the binding energy (E_B) of ~282.5 eV is observed from

the bulk of SiC substrate and the other peak S1 at the higher binding energy of ~284.3 eV may originate from the surface C-C bond, namely, the S1 component may indicate the presence of s-p^2 hybridized C-C bonds. Consequently, the peak S1 may be associated with the C-enriched surface.
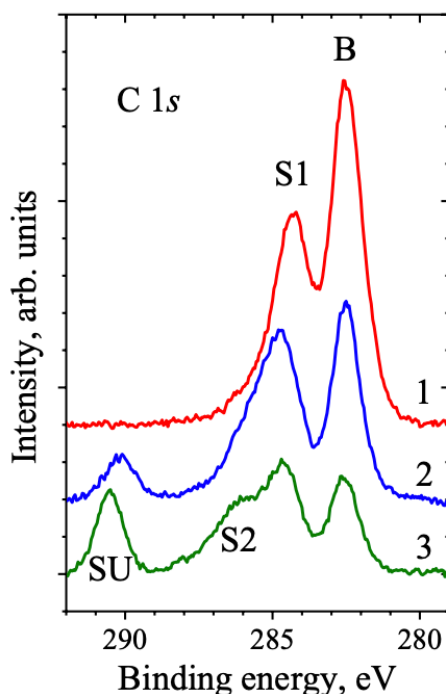

Fig. 1. Photoemission spectra of the C 1s core level recorded from the Ba/SiC/Si(111)-8° interface at different Ba coverages: 1—clean surface (Ba-free surface), 2—0.5 ML, 3—1.0 ML. Excitation energy $h\nu$ = 450 eV

A cardinal change in the C 1s core level spectrum is revealed upon Ba adsorption on the SiC(111)-8°surface (Fig. 1, curves 2, 3). The appearance of an additional surface component S2 at the binding energy of ~286.0 eV is found at the initial stage of Ba adsorption at 0.5 ML (Fig. 1, curve 2). An odd effect is the appearance of a new peak SU at the E_B of ~290.5 eV at the highest binding energy side of the B, S1 and S2 peaks. It can be seen that the binding energies of S2 and SU components show a weak dependence on the Ba coverage and the relative intensities are equally modified with the increase of Ba coverage. Several components appear at the higher binding energies that indicate a degree of interaction between C-C atoms and an increase in the ionicity of C. The presence of S1 and S2 components is an evidence for the corrugation of the vicinal SiC(111)-8°surface. The positive shift of the S2 component under Ba adsorption is obtained to be ~3.5 eV. This indicates a higher charge transfer from the C surface atoms to the Ba adsorbed atoms.

An uncommon modification of the C 1s spectrum is observed after one monolayer of Ba adsorption on the SiC(111)-8° surface (Fig. 1, curve 3), namely, a supplementary SU peak at the energy of ~290.5 eV. Note that both the S2 and SU peaks arise simultaneously and increase in intensity. The SU peak is peculiar as it differs from the traditional C 1s core level spectrum. The SU component can be identified as a shake-up satellite. The shake-up satellite is a well-known characteristic of the photoemission process in graphitic and aromatic systems. The shake-up is a two-electron phenomenon; the emitted photoelectron with E_B of 286.0 eV (peak S2) can excite a transition resulting in an additional peak SU at the higher binding energy of 290.5 eV (peak SU). Graphitic systems show a shake-up peak shifted toward higher binding energy from the main peak. Therefore, the modification of the surface structure of the vicinal SiC(111)-8° surface due to Ba adsorption indicates 2D phase transition. It is found that 2D surface phase transition from the C-enriched SiC(111)-8° surface to the aromatic-like one originates from the Ba atomic layer deposition. The result may be due to the charge transfer to C atoms located in interface area in the process of Ba adsorption.

It is possible to suppose that we deal with a graphene-like surface layer comprising a high proportion of sp^3 hybridized C-C bonds at the vicinal SiC surface. It is also possible to assume that the surface reconstruction induced by Ba adsorption can create the sp^2, sp^3 and $\pi \rightarrow \pi^*$ hybridized C-C bonding inherent aromatic-like compounds. Therefore, it can be confirmed that 2D phase transition on the vicinal SiC surface takes place due to Ba adsorption which leads to the creation of the C-C chemical bonds close in nature to the bonds inherent in aromatic-like compounds.
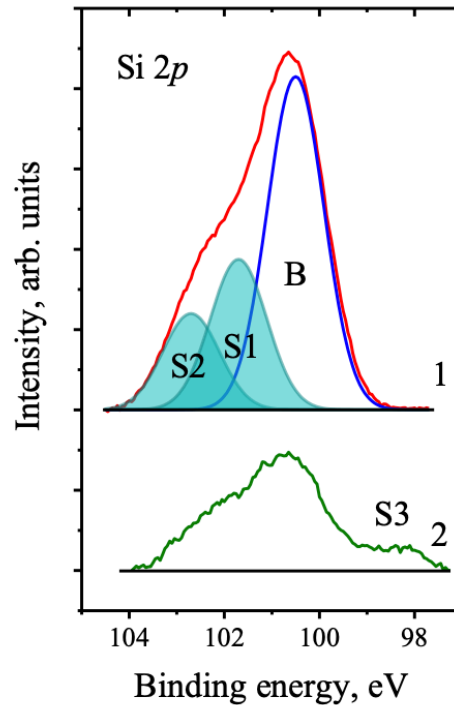

Fig. 2. The Si 2*p* core level photoemission spectra for SiC(111)-8° surface (1) and Ba/SiC(111)-8° interface at Ba coverage of 0.8 ML (2). Excitation energy *hν* = 130 eV

Figure 2 represents the modification of the Si 2*p* core level spectrum under Ba adsorption on the SiC(111)-8° surface recorded at the excitation photon energy of *hν* = 130 eV. The bulk-related peak B at the binding energy of ~100.5 eV corresponds to the Si 2*p* components (the spin-orbit-split Si $2p_{1/2}$ and Si $2p_{3/2}$ states are unresolved in the spectra). Two surface-related components S1 and S2 at higher binding energies are found for the clean SiC(111)-8° surface (Figure 2).

The component labeled S1 (E_B = ~101.7 eV) is most easily seen in the surface sensitive spectra. It most probably originated from Si surface atoms. The S2 component (E_B = ~102.7 eV) appears as a shoulder on the high binding energy side of the B and S1 peaks and, most likely, can be connected with the Si-Si surface dimmers. Ba adsorption leads to the suppression of B, S1 and S2 peaks. The appearance of the component S3 (E_B = ~98.5 eV) is most probably associated with the so-called interfacial states provided by interaction of Ba-Si atoms in the buffer layer between the C-enriched surface layer and the SiC substrate.

Findings

In summary, first, the Ba/SiC(111)-8° interface has been studied in detail *in situ* using photoelectron spectroscopy with photon energies in the range of 100–450 eV. The SiC(111)-8° samples were grown by an original method of epitaxy of low-defect unstressed nanoscaled silicon carbide films. Second, experimental data show that the aromatic-like nanostructure can be created exclusively on the vicinal SiC(111)-8° surfaces in the presence of stabilizing adsorbed metal atoms, specifically, Ba atoms. It is shown that the surface nanoclusters are formed due to the local interaction between silicon vacancies, carbon atoms and Ba adatoms. It is established that the carbon C-clusters are composed of carbon rings

and their chemical bonds are similar in nature to the bonds in aromatic-like compounds. Third, the modification of the Si 2*p* core level spectrum with surface-related components indicates a compound surface atomic structure that can provide two features S1 and S2 associated with Si surface atoms and Si surface dimmers. The appearance of the S3 component is most probably associated with the so-called interfacial states due to the interaction of Ba with Si atoms.

Acknowledgements

References

Abavare, E. K. K., Iwata, J.-I., Oshiyama, A. (2013) Atomic reconstruction and electron states at interfaces between 3C-SiC(111) and Si(110). *Physical Review B: Covering Condensed Matter and Materials Physics*, 87 (23), article 235321. DOI: 10.1103/PhysRevB.87.235321 (In English)

Bechstedt, F., Furthmüller, J. (2004) Electron correlation effects on SiC(111) and SiC(0001) surfaces. *Journal of Physics: Condensed Matter*, 16 (17), S1721–S1732. DOI: 10.1088/0953-8984/16/17/014 (In English)

Benemanskaya, G. V., Dement'ev, P. A., Kukushkin, S. A., Osipov, A. V., Timoshnev, S. N. (2019a) A new type of carbon nanostructure on a vicinal SiC(111)-8° surface. *Technical Physics Letters*, 45 (3), 201–204. DOI: 10.1134/S1063785019030039 (In English)

Benemanskaya, G. V., Dement'ev, P. A., Kukushkin, S. A., Osipov, A. V., Timoshnev, S. N. (2019b) Carbon-based aromatic-like nanostructures on the vicinal SiC surfaces induced by Ba adsorption. *ECS Journal of Solid State Science and Technology*, 8 (6), M53–M59. DOI: 10.1149/2.0031906jss (In English)

Bosi, M., Attolini, G., Negri, M. et al. (2013) Optimization of a buffer layer for cubic silicon carbide growth on silicon substrates. *Journal of Crystal Growth*, 383, 84–94. DOI: 10.1016/j.jcrysgro.2013.08.005 (In English)

Eddy, C. R. Jr., Gaskill, D. K. (2009) Silicon carbide as a platform for power electronics. *Science*, 324 (5933), 1398–1400. DOI: 10.1126/science.1168704 (In English)

King, S. W., Nemanich, R. J., Davis, R. F. (2015) Photoemission investigation of the Schottky barrier at the Sc/3C-SiC(111) interface. *Physica Status Solidi: Basic Solid State Physics*, 252 (2), 391–396. DOI: 10.1002/pssb.201451340 (In English)

Kukushkin, S. A., Osipov, A. V. (2013) A new method for the synthesis of epitaxial layers of silicon carbide on silicon owing to formation of dilatation dipoles. *Journal of Applied Physics*, 113 (2), article 024909. DOI: 10.1063/1.4773343 (In English)

Kukushkin, S. A., Osipov, A. V. (2014) Theory and practice of SiC growth on Si and its applications to wide-gap semiconductor films. *Journal of Physics D: Applied Physics*, 47 (31), article 313001. DOI: 10.1088/0022-3727/47/31/313001 (In English)

Okuda, T., An, K.-S., Harasava, A., Kinoshita, T. (2005) Structural analysis of Ba-induced surface reconstruction on Si(111) by means of core-level photoemission. *Physical Review B: Covering Condensed Matter and Materials Physics*, 71 (8), article 085317. DOI: 10.1103/PhysRevB.71.085317 (In English)

Su, J., Niu, Q., Tang, C., Zhang, Y., Fu, Z. (2012) Growth of void-free 3C-SiC films by modified two-step carbonization methods. *Solid State Sciences*, 14 (4), 545–549. DOI: 10.1016/j.solidstatesciences.2012.01.017 (In English)

Takahashi, R., Handa, H., Abe, S. et al. (2011) Low-energy-electron-diffraction and X-ray-phototelectron-spectroscopy studies of graphitization of 3C-SiC(111) thin film on Si(111) substrate. *Japanese Journal of Applied Physics*, 50 (7R), article 070103. DOI: 10.1143/JJAP.50.070103 (In English)

Virojanadara, C., Hetzel, M., Johansson, L. I., Choyke, W. J., Starke, U. (2008) Electronic and atomic structure of the 4H-SiC(102)-c(2x2) surface. *Surface Science*, 602 (2), 525–533. DOI: 10.1016/j.susc.2007.11.012 (In English)

Wang, J., Zhang, L., Zeng, Q. et al. (2009) Adsorption of atomic and molecular oxygen on 3C-SiC(111) and ($\overline{1}\overline{1}\overline{1}$) surfaces: A first-principles study. *Physical Review B: Covering Condensed Matter and Materials Physics*, 79 (12), article 125304. DOI: 10.1103/PhysRevB.79.125304 (In English)

Watcharinyanon, S., Johansson, L. I., Xia, C., Virojanadara, C. (2012) Changes in structural and electronic properties of graphene grown on 6H-SiC(0001) induced by Na deposition. *Journal of Applied Physics*, 111 (8), article 083711. DOI: 10.1063/1.4704396 (In English)

Watcharinyanon, S., Virojanadara, C., Johansson, L. I. (2011) Rb and Cs deposition on epitaxial graphene grown on 6H-SiC(0001). *Surface Science*, 605 (21–22), 1918–1922. DOI: 10.1016/j.susc.2011.07.007 (In English)

UDC 536.42+539.19   DOI: 10.33910/2687-153X-2020-1-3-113-122

Comparative analysis of semiconductor-metal phase transition mechanisms in vanadium oxides (V$_2$O$_3$ and VO$_2$)

A. V. Ilinskiy$^{\boxtimes 1}$, E. I. Nikulin[1], E. B. Shadrin[1]

[1] Ioffe Institute, 26 Politekhnicheskaya Str., Saint Petersburg 194021, Russia

Authors

Aleksandr V. Ilinskiy, e-mail: Ilinskiy@mail.ioffe.ru

Evgeniy I. Nikulin

Evgeniy B. Shadrin, ORCID: 0000-0002-1423-2852

Abstract. In this study, phase transformation mechanisms in thin V$_2$O$_3$ and VO$_2$ films are analysed based on experimental data and on the qualitative model for vanadium oxides proposed by the authors of the study. New features of semiconductor-metal phase transformation mechanism revealed in V$_2$O$_3$ are discussed. Characteristics of phase transition process in V$_2$O$_3$ is compared with the features of a similar phase transformation in thin VO$_2$ in detail.

Keywords: vanadium oxides, Magneli phases, semiconductor-metal phase transition, phase transformations, correlation energy.

Introduction

Recently, there has been a revival of interest in studying Semiconductor-Metal Phase Transition (SMPT) in vanadium oxides in the Magneli series: VO$_2$, V$_2$O$_3$, V$_6$O$_{13}$, V$_3$O$_5$, V$_4$O$_7$, V$_6$O$_{11}$, etc. This interest is due to unusual results for vanadium dioxide obtained using modern research methods: optical, femtosecond and dielectric spectroscopy (Wegkamp, Stähler 2015; Ilinskiy et al. 2020), spectroscopy of vanadium-oxide photonic crystals (Fan et al. 2015; Golubev et al. 2001; Lu, Zhao 2012; Ye et al. 2015), atomic force microscopy (Tselev et al. 2013), micro-Raman light scattering (Schilbe 2002) and others. Such studies have resulted in a comprehensive understanding of the processes that occur during phase transition in vanadium oxides.

However, such comprehensive understanding only exists for vanadium dioxide. Analysis of the mechanisms of phase transformations in other oxides of the Magneli series has to a large extent been neglected by researchers. Therefore, in this work, the main focus is on vanadium sesquioxide (V$_2$O$_3$), a compound possessing a number of unusual physical properties. It seems reasonable to consider these unusual properties by comparing them with the properties of the well-studied VO$_2$ (temperature SMPT T_c = 340 K).

SMPT also occurs in V$_2$O$_3$ with increasing temperature, but it occurs at lower temperatures than in VO$_2$ (at T_c = 140 K < T_c = 340 K). Moreover, the increase in the electrical conductivity of V$_2$O$_3$ after phase transition is much larger (for a single V$_2$O$_3$ crystal, the change is 7 orders of magnitude, and in VO$_2$ it is 4 orders of magnitude). There is no doubt that these differences are associated with differences in vanadium oxide crystal structure. It is crucial to note that vanadium atom has an unfinished

d-shell, and also that strong interactions between electrons play an important role in the phase transition when the energy structure of the crystal is rearranged.

Namely, a strong temperature dependence of the semiconductor energy gap width is associated with correlation effects in V_2O_3 and VO_2 compounds (Gatti et al. 2007). In such materials, the position of energy bands depends on their occupancy by electrons. Since V_2O_3 and VO_2 are oxides of V, a transition metal (No. 23 in the periodic table), they exhibit a fundamental property of vanadium: the dependence of the energy position of atomic levels on their electron occupancy. This conclusion is confirmed by the analysis of electronic configurations of Ti, V, and Cr, i.e. elements located in the 4th period of the table.

Namely, during the transition from element 22 (Ti with $3d^2 4s^2$ configuration) to element 23 (V with $3d^3 4s^2$ configuration), the 3*d* shell is filled with electrons. But when going to element 24 (Cr: $3d^5 4s^1$), the filling sequence is violated. This is due to the fact that the additional electron acquired by Cr greatly reduces the energy of the 3*d* level and initiates a transition of an electron from the 4*s* level to the 3*d* level. The reasons for the lower 3*d* level energy in V and Cr atoms are the strong interactions between the electrons. These interactions take place simultaneously with the interaction of electrons with the V nucleus. The ability of V levels to lower energy when they are occupied by electrons is transferred to vanadium oxides, in which the positions of the bands on the energy scale are also dependent on their electron occupancy.

Despite the persuasiveness of these arguments, the specific details of V_2O_3 and VO_2 electronic spectrum and crystal structure transformation during the phase transition are of great interest, and for V_2O_3 they still remain unclear.

The objective of this work, therefore, was to study the features of the phase transition in nanocrystallites of thin V_2O_3 films in detail, as well as to compare these features with well-studied features of SMPT in thin VO_2 films.

General information on the physical properties of V_2O_3 and VO_2 single crystals

Vanadium sesquioxide V_2O_3

The V_2O_3 crystal lattice is a corundum (Al_2O_3) type lattice (Tan et al. 2012). The unit cell of the rhombohedral (trigonal) phase contains 4 vanadium atoms and 6 oxygen atoms (V_4O_6). In the V_2O_3 lattice, for every two oxygen octahedra containing V^{3+}, one octahedron does not contain the V^{3+} ion. Such octahedra with empty bases are located on both sides of a pair of octahedra with filled bases. The coordination number of the V^{3+} ion is 6, the coordination number of the O^{2-} ion is 4.

In V_2O_3 single crystals, SMPT occurs at an increased temperature of $T_c = 140$ K. In this case, single crystal symmetry rises from monoclinic to rhombohedral (trigonal) (Nagaosa et al. 2010). The band gap in the semiconductor low-temperature phase is estimated at $E_g = 0.3$ eV (Keller et al. 2004).

Vanadium Dioxide VO_2

The crystal lattice of the VO_2 metal phase has tetragonal symmetry, while the semiconductor lattice has monoclinic symmetry (Shimazu et al. 2015). The unit cell contains 2 vanadium atoms and 4 oxygen atoms, (V_2O_4). In the VO_2 lattice, all oxygen octahedra contain vanadium atoms in the centres of their bases. The coordination number of the V^{4+} ion is 6, the coordination number of the O^{2-} ion is 3.

In vanadium dioxide single crystals, SMPT occurs with the temperature increase to $T = 340$ K. The band gap in the semiconductor low-temperature phase is estimated at $E_g = 0.7$ eV.

SMPT in V_2O_3 and VO_2 films

This work is focused, as indicated above, on the study of phase transition in thin films of vanadium oxides consisting of crystallites with sizes of tens of nanometers. Therefore, when describing the phase transition process, it should be taken into account that the grains of V_2O_3 and VO_2 films have different sizes, which follow a normal distribution. As such, grains differ from each other by the contributions of surface energy to the phase transition process, and, consequently, differ in phase transition temperatures, the width and shape of the elementary hysteresis loops and the degree of grain adhesion to the substrate. It follows that all of the above factors have to be taken into account to describe the SMPT mechanism in nanocrystalline films. At the initial stage of phase transition modelling, this work will only

discuss the features of SMPT in individual nanocrystallites, while at the final stage it will be possible to make phase transition in the entire film as a whole.

Samples

The samples were thin (about 70 nm thickness) V_2O_3 and VO_2 films synthesized by laser ablation method on a SiAl ceramic substrate. For optical experiments, films synthesized on a mirror aluminum layer preliminarily deposited on a SiAl substrate were used. A thin-film optical interferometer arose. The use of such a thin-film Fabry–Pérot interferometer allows one to enhance the effect of a change in the reflection coefficient of the film structure during a phase transition.
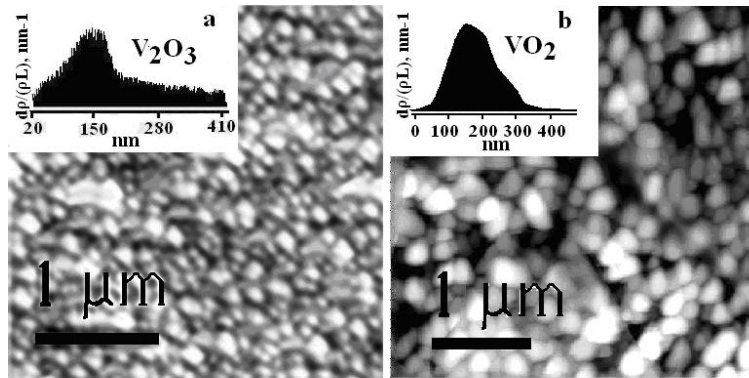

Fig. 1. The atomic force image of V_2O_3-a and VO_2-b films

Figure 1 shows the AFM images of V_2O_3 and VO_2 films. A comparison of the images shows that the films have a uniform granular structure with a typically occurring grain size of 150–200 nm. At the same time, histograms show that the grain size of the films is distributed. The shape and width of the temperature hysteresis loops of the films as a whole depends on the size distribution.

The results of the experiments

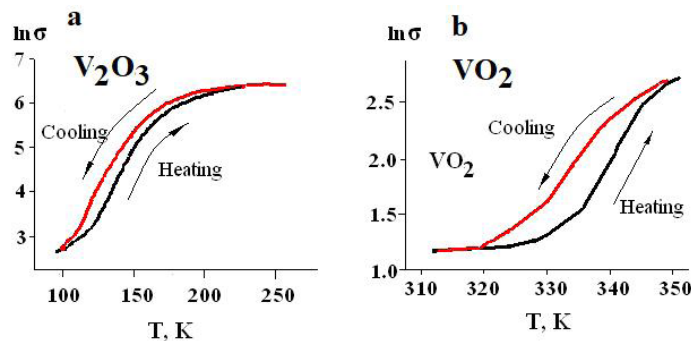*Temperature hysteresis loops of the electrical conductivity of films*

Fig. 2. The temperature hysteresis loops σ of the film V_2O_3-a, and VO_2-b

Figure 2a shows temperature dependence of electrical conductivity $(\ln\sigma(T))$ of the V_2O_3 film obtained by us. The graphs show that electrical conductivity of the film increases by more than an order of magnitude with an increase in temperature from 100 to 300 K. At high temperatures, the conductivity is metallic with a weak decrease of conductivity with increasing temperature deep into the metal phase. This is typical of metals. In the heating-cooling cycle, a hysteresis loop extended in temperature is observed (the length of the loop branches is ~120 K). The width of the loop is 7 K, the *centre of gravity* of the branch of the loop corresponding to heating falls onto the temperature $T_c = 140$ K. This temperature is to a first approximation taken as the temperature of SMPT.

A detailed analysis shows that the value of T_c depends on the size of the crystallites of the film and the degree of imperfection of their crystal structure. Specifically, due to the size distribution of grains, they differ in the widths of the elementary hysteresis loops out of which the main loop is composed. The difference in loop widths indicates the martensitic nature of SMPT in V_2O_3. In addition, a difference in the degree of defectiveness of the grains, for example, a difference in the concentration of oxygen vacancies in film grains, creates a difference in the equilibrium temperatures of the T_c phases in these grains. This is due to the correlation nature of that part of SMPT, which is the Mott electronic phase transition (Gatti et al. 2007). The fact is that oxygen vacancies are electron donors that lower T_c. The shape of hysteresis loop branch, which corresponds to heating and whose *centres of gravity* are taken as the temperature of the phase transition of the film, is determined as the temperature of an infinite percolation conduction cluster formation. It follows that the numerical value of T_c only on average characterizes the temperature of the phase transition in the V_2O_3 film.

It is also important to note here that during the hydrogenation of V_2O_3 film, the entire temperature hysteresis loop shifts toward low temperatures by 4–6 K by the atomic % of embedded hydrogen (Andreev et al. 2017). This circumstance will be used in discussing SMPT mechanisms in the studied film structures.

Figure 2b shows the temperature dependence of the electrical conductivity of VO_2 film. Here, during the phase transition, the electrical conductivity increases by an order of magnitude, and at large T_c temperatures, it is of a metallic nature. But the branches of the hysteresis temperature loop are less extended (30 K), and the loop width is 12 K. Here, when the film is hydrogenated, the entire temperature hysteresis loop shifts toward lower temperatures, but by a larger value than V_2O_3: 10–15 K (Ilinskiy et al. 2011).

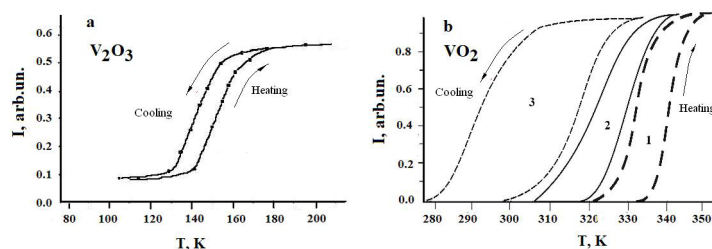*Temperature hysteresis loops of film optical reflectivity*

Fig. 3. Temperature hysteresis loops of the intensity of light reflected from films: a — V_2O_3 and b — VO_2 (1 — the initial loop, 2 — after annealing in vacuum for 15 min. at 250°C, 3 — after annealing in vacuum for 15 min. at 350ºC)

Figure 3a demonstrates temperature dependence of optical reflectance (I(T)) of the V_2O_3 film obtained by us. The graphs show that the intensity of light reflected from the film increases by more than an order of magnitude with temperature increase from 100 to 300 K. Therefore, we can assume that at high temperatures the film grains are in the metal phase. In the heating-cooling cycle, an intensity hysteresis loop of the light reflected from the film is observed. It is high and extended along temperature (~120 K). The width of the loop is 7 K, the *centre of gravity* of the branch of the loop corresponding to the heating of the sample also falls on the temperature T_c = 140 K.

Figure 3b shows temperature dependence of optical reflectivity of VO_2 film for an *ordinary* film (curve 1). Here, during a phase transition, the intensity of the light reflected from the film increases by an order of magnitude, and at high temperatures the conductivity is metallic. However, the thermal hysteresis loop is less extended in temperature (30 K), and its width is 12 K. In Fig. 3b, loops 2 and 3 were obtained for a film treated in a special way: the film was vacuum annealed. The treating process is described in more detail in the signature to Fig. 3. The figure shows that after this treatment, the hysteresis loops shift to the low-temperature region.

The optical reflectivity of V_2O_3 and VO_2 films is also characterized by the fact that during the hydrogenation of films, all temperature hysteresis loops are shifted toward low temperatures by 10–15 K (Andreev et al. 2017; Ilinskiy et al. 2011).

Acoustic emission

During SMPT, V_2O_3 and VO_2 films exhibit effective acoustic emission in the immediate vicinity of T_c (Andreev et al. 2000; McBride et al. 1974). This fact is interesting for detailing the processes of phase transformations in these oxides.

Hall constant

For V_2O_3, we measured the Hall constant R_h at low (T = 95 K) and high (T = 300 K) temperatures: R_h = 1200 cm³/K and R_h = 1.3 cm³/K, respectively. For VO_2, the Hall constant obtained by us at low (T = 100 K) and high (T = 380 K) temperatures turned out to be R_h = 6000 cm³/K and R_h = 0.6 cm³/K, respectively. The numerical values of the Hall constant indicate a large increase of the concentration of free electrons in both oxides with increasing temperature.

Discussion of the results

Peierls semiconductor-metal structural phase transition

Peierls phase transition is a change in the symmetry and parameters of the crystal lattice during the formation (destruction) of V-V dimers. Dimer is a system of two V ions coupled in a pair located in neighbouring octahedra. This takes place both in V_2O_3 and in VO_2. Each V ion gives one electron, which is free from the formation of a skeleton, to create a strong σ-bond with the V ion of the neighbouring octahedron in both oxides. Another free electron of the V^{3+} ion, which exists only in V_2O_3, creates, in addition, a strong π-bond with the neighbouring V^{3+} ion. As the temperature decreases (increases), new bonds that are not capable of (destroying) the temperature factor kT arise (disappear) between the atoms of the lattice, i.e., new dimers arise (or are destroyed). When the critical concentration of arising (destroyed) dimers is reached, the symmetry of the entire lattice of the single crystal changes abruptly. The Peierls thermal phase transition in the films of vanadium oxides discussed here has hysteresis with a loop width of the order of several degrees. The large loop width is due to the fact that the small sizes (100–200 nm) of the nanocrystallite films make, according to the Laplace theorem, a significant contribution of surface energy to the energy of SMPT. Namely, the contribution of surface energy to the energy of SMPT is so large that a deviation of several phase equilibrium temperatures T_c is required to complete the phase transition. This effect occurs both when the temperature changes in the direction of the metal phase, and in the direction of the semiconductor phase (Aliev et al. 2006). Let us consider in more detail the process of phase transition in V_2O_3 and VO_2 nanocrystallites.

Vanadium sesquioxide V_2O_3

Figure 4 shows the bases of ten octahedra of the V_2O_3 crystal lattice, in the centres of which V^{3+} ions are located adjacent to each other. These ions form π-bonds between each other due to overlapping $3d_{xz}$-$3d_{x'z'}$ and $3d_{yz}$-$3d_{yz}$ branches of vanadium ion orbitals.

The vanadium atom, located in the centre of the base of the oxygen octahedron, forms $3d_{xy}$-bonds with six oxygen atoms due to its $3d^1_{xy}(1)3d^0_{z2}(1)4s^2(1)4p^0(3)$ hybridization (the superscript is the number of electrons in the orbitals). During the formation of the lattice, a vanadium atom gives on average ½ of its electron density to the oxygen atoms of the environment and turns into a V^{3+} ion. At the same time, each oxygen atom forms four $2s^2(1)2p_x^1(1)2p_y^1(1)2p_z^2(1)$-hybrid orbitals and gives 3/2 of its electron density in connection with vanadium atoms. It forms four complete σ-bonds with vanadium atoms in the centres of the bases of the surrounding octahedra (2 electrons per bond). And the V^{3+} ion creates 6 full-fledged σ-bonds with oxygen ions of its own octahedron. Thus, a strong octahedral V_2O_3 framework is formed.

Since, to ensure the strength of the crystal lattice, each V^{3+} ion gives only 3 electrons to the formation of σ-bonds (one from $3d^1_{xy}$ and two from the $4s^2$ orbitals), each V^{3+} ion has two electrons not used to form bonds with O^{2-} ions - octahedron. Due to the participation of one unoccupied electron, a strong σ-bond is formed between $3d_{x2-y2}$-$3d_{x2-y2}$ orbitals of V^{3+} ions, which are located at the bases of neighbouring octahedra. Durable $3d_{x2-y2}$-$3d_{x2-y2}$ σ-dimers appear in V_2O_3, which are not destroyed either in the semiconductor or in the metal phases (see the lower part of Fig. 4).
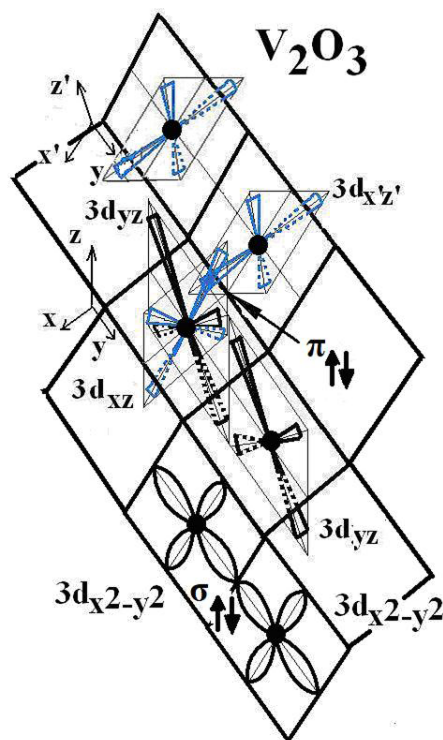
Fig. 4. Fragment of V_2O_3 crystal lattice illustrating the formation of dimers. The upper part of the figure shows the formation at $T < T_c$ of stable π-dimers formed from the dynamic $3d_{xy}$-$3d_{x'y'}$s bonds existing at $T > T_c$. The lower part of the figure shows σ-$3d_{x2-y2}$-$3d_{x2-y2}$-dimers stable in V_2O_3 at temperatures both larger and lower than T_c

Electron density corresponding to the second free electron of the V^{3+} ion in the metal phase is uniformly distributed between the $3d_{xz}$ and $3d_{yz}$ orbitals of the vanadium ion in the octahedron. Due to the overlapping branches of the orbitals of the V^{3+} ion of neighbouring octahedra (Fig. 4), V-V pairs arise, connected by π-bonds. A set of such dynamic π-bonds perpendicular to each other creates a one-dimensional zigzag structure along the hexagonal axis C_R, the elements of which are interconnected. Since each V^{3+} ion gives away only one free electron (another is used to create a non-destructive σ-bond), in V_2O_3 there is a system of one-dimensional zigzag filaments created with metallic type conductivity. The value of the Hall constant measured by us unambiguously indicates electronic type of conductivity.

The lattice of the semiconductor V_2O_3 phase has monoclinic symmetry, which contains fewer symmetry elements than the metal phase of rhombohedral symmetry. This is due to the fact that at temperatures lower than T_c, π-dimers are formed. In such dimers, V^{3+} ions are located in the metal phase at the base centres of neighbouring octahedra, which are inclined to each other at an angle of 150°. With SMPT, V^{3+} ions exit base centres and approach each other.

The reason for vanadium ions leaving base centres is that due to the tilt, the overlap of the branches of $3d_{xz}$ and $3d_{x'z'}$- orbitals in $3d_{x'z'}$-$3d_{xz}$-π- bonds is 60% larger than that of $3d_{yz}$-$3d_{yz}$-π-bonds. From this, according to the theory of molecular orbitals, it follows that the binding energy of $3d_{x'z'}$-$3d_{xz}$-π dimers is almost twice as high as the binding energy of $3d_{yz}$-$3d_{yz}$-π dimers, and the distance between the centres of V^{3+} ions is 37% less. The consequence of this is the formation of precisely $3d_{x'z'}$-$3d_{xz}$-π-dimers and a doubling of the repetition period of the peaks of the thermodynamic potential of the one-dimensional system of π-dimers, where C_R. $3d_{xz}$-$3d_{x'z'}$-π-dimers with a higher binding energy than $3d_{yz}$-$3d_{yz}$-π-dimers also capture a single free electron. This excludes the participation of $3d_{yz}$-$3d_{yz}$-π bonds in conductivity. The low-temperature monoclinic phase V_2O_3 acquires sharply reduced conductivity.

In the crystal lattice, the energy levels corresponding to the binding (π) and loosening (π*) of orbitals expand on the energy scale in the π and π* zones, which differ sharply in their energy positions in the conducting and semiconductor phases (Fig. 5). It is crucial that in the semiconductor phase, a gap appears on the energy scale between binding $3d_{xz}$-$3d_{x'z'}$π-band and binding $3d_{yz}$-$3d_{yz}$-π band (experimentally estimated by Eg = 0.3 eV (Keller et al. 2004)). Thus, the V_2O_3 crystal is in the low-temperature phase a semiconductor with a band gap of 0.3 eV.

The aforesaid is illustrated in Fig. 5a, which shows a diagram of energy bands of low-temperature V_2O_3 semiconductor phase.
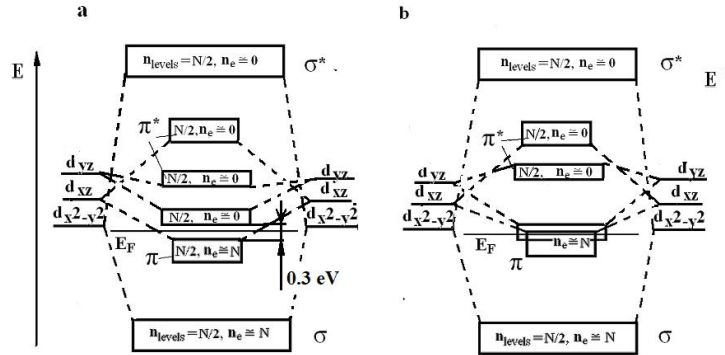

Fig. 5. Diagram of energy zones of V_2O_3 crystal. a — semiconductor phase, b — metal phase

Vanadium Dioxide VO_2

Vanadium V^{4+} ion in each oxygen octahedron, resulting from $3d^1_{xy}(1)3d^1_{z2}(1)4s^2(1)4p^0(3)$ hybridization of vanadium atom, forms 6 σ-bonds with O^{2-} ions, which arise during $2s^2(1)2p_x^1(1)2p_y^1(1)$ hybridization of an oxygen atom. Each oxygen atom is connected by 3—but not 4, as in V_2O_3—σ-bonds with V^{4+} ions, which are located in neighbouring octahedra. The V^{4+} ion gives an average of 4/3 of its electron density to the σ-bond with O^{2-}, which gives an average of 2/3 to the σ-bond. A complete V-O σ-bond arises, having two electrons with oppositely directed spins.

In VO_2 metal phase, each V-octahedron has one free electron per V^{4+} ion, which is not involved in the stabilization of the lattice framework. This electron is located on $3d_{x2-y2}$ orbital, which is located in the plane of the base. The cruciform branches of this orbital are parallel to the ribs of the base of the frame. V^{4+} ions form a system of one-dimensional filaments along the tetragonal axis C_R, which creates a one-dimensional metal-type conductivity in a half-filled energy zone. This zone arises in VO_2 when the energy level corresponding to the $3d_{x2-y2}$ orbitals expands in crystal to zone. The number of energy levels in such zone is equal to the number of V^{4+} ions and, at the same time, is equal to the number of electrons in the zone. Due to Pauli exclusion principle, electrons occupy only half of the levels of the lower part of the zone. The upper half of the zone remains free. This corresponds to the metallic conductivity of the material in high-temperature phase.
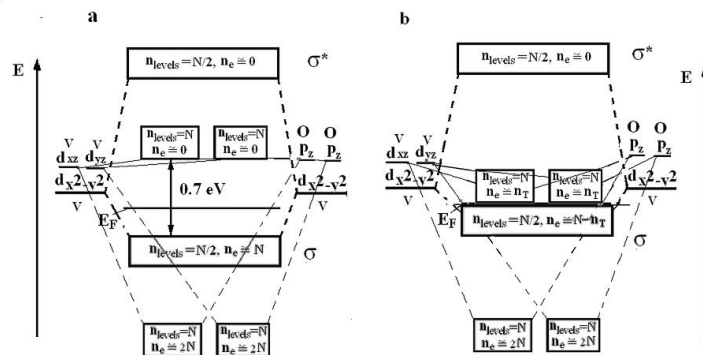

Fig. 6. Diagram of the energy zones of the VO_2 crystal. a — semiconductor phase, b — metal phase

In low-temperature VO_2 phase of monoclinic symmetry a $3d_{x2-y2}$ orbitals of neighbouring octahedra form $3d_{x2-y2}$-$3d_{x2-y2}$ σ-dimers due to the fact that the temperature factor is not enough to destroy them, as it was in the metal phase. Therefore, V^{4+} ions are pairwise shifted towards each other and the period of repetition of the thermodynamic potential along C_R doubles. The crystal conductivity sharply

decreases, and the material acquires semiconductor properties (EG = 0.7 eV), since free electrons are now fixed in $3d_{x2-y2}$-$3d_{x2-y2}$ σ bonds. A structural phase transition to low-symmetry phase occurs.

Fig. 6a is a diagram of the energy zones of low-temperature semiconductor VO_2 phase.

Mott electronic semiconductor-metal phase transition

The Mott phase transition represents a continuous increase in the metallization of a single crystal with an increase of crystal's temperature, which was in a semiconductor state with E_g = 0,7 eV. In this case, a change in the symmetry of the crystal lattice does not occur. With increasing temperature, the concentration of free electrons in the conduction band of the semiconductor continuously increases. The main feature of the Mott phase transition is that experimental data indicates a—very marked— decrease of the band gap of the semiconductor when the transition is completed. When the temperature reaches a critically high value, the energy gap of the semiconductor becomes equal to zero. The semiconductor goes into a metallic state with a lattice that maintains a low symmetry of the semiconductor phase. This second-order phase transition does not have thermal hysteresis. However, in the vanadium oxides studied by us, the Peierls and Mott phase transitions do not occur in the "pure state". The actual situation is more complicated: when the temperature changes, both phase transitions occur. Moreover, they mutually influence each other. Common schemes of the process of making SMPT in V_2O_3 and VO_2 in the first approximation coincide.

The key finding is that in both oxides, electrons obeying the Fermi distribution cannot receive energy greater than 30 meV at temperatures below T_c, which does not allow efficient transfer through the energy gap (0.3 eV for V_2O_3 and 0.7 eV for VO_2) of such a number of electrons that is necessary for the transition of the material from semiconductor into metallic phase. Such transition is possible when a critical number of dimers that stabilize the semiconductor phase are destroyed ($3d_{xz}$-$3d_{x'z'}$-π dimers for V_2O_3 and $3d_{x2-y2}$-$3d_{x2-y2}$-σ-dimers for VO_2). From the bonds of these dimers, there is a transfer of electrons to the allowed band. It follows that V_2O_3 and VO_2 must remain semiconductors even at room temperature. This, however, conflicts with the results of the experiment. The contradiction is eliminated by Mott's fundamental idea, where phase transition energy has to include high correlation energy of interaction between the electrons moving in the periodic potential of the crystal lattice. According to Mott (Mott 1990), the transfer of electrons into the conduction band causes it to lower in energy, which then increases the transfer of new electrons. This causes additional zone lowering, etc. The zone from which the electrons leave, on the contrary, rises in energy (Gatti et al. 2007). It follows that the standard thermal transfer of electrons into the conduction band of a semiconductor from its valence band with increasing temperature causes a decrease in the band gap if correlation interaction between the electrons exists. At the same time, the concentration of electrons in the conduction band increases. This process is a temperature-extended Mott semiconductor-metal phase transition.

Figures 5 and 6 illustrate the aforesaid. They show the energy diagrams of the bands in the semiconductor and metal phases for both vanadium oxides.

This process in both oxides leads to effective destruction of dimers stabilizing the semiconductor phase and which, according to the theory of valence bonds, serve as electron donors. The semiconductor phase in both oxides rapidly passes into the metallic phase (Peierls transition) upon reaching a critical number of destroyed dimers. Thus, in each grain of the vanadium oxide film, Peierls structural transition is initiated by Mott electronic transition. That is, dimers that remain undisturbed cannot keep the crystal lattice in a state of low symmetry. In all grains, the Peierls phase transition occurs at different temperatures—T_c in a defect-free crystal—depending on their size.

The presence of correlation effects is additionally confirmed by the fact that during VO_2 film annealing in vacuum, the hysteresis loops shift to lower temperatures (Fig. 3b, curves 2, 3). Specifically, during vacuum annealing, oxygen vacancies are formed, which are electron donors. Donor electrons pass into the conduction band. Due to correlation effects, the conduction band decreases in energy, while the band gap and T_c narrow. Hydrogenation of the films also leads to the shift in the temperature hysteresis loops toward lower temperatures in both V_2O_3 and VO_2. Indeed, introduced hydrogen, it being an electron donor, transfers free charge carriers to the conduction band, causing additional correlation lowering in energy and a decrease in T_c.

The destruction of π-dimers (V_2O_3) and σ-dimers (VO_2) with increasing temperature leads to a decrease in the number of dimers to a critical level, so that they cannot keep the lattice in a state of low symmetry. After that, an abrupt Peierls structural transition occurs. Vanadium ions move in an avalanche-

like direction toward the centres of oxygen octahedra under the influence of the valence forces of the oxygen skeleton. All of crystallite dramatically changes its symmetry and size. In both oxides, a strong acoustic emission arises (Andreev et al. 2000; McBride et al. 1974).

Crucially, it should be noted that acoustic emission in single crystals of both oxides is observed after T_c is reached both when the temperature moves deep into the metal phase and after T_c is reached when the temperature moves deep into the semiconductor phase. This directly indicates the displacement of V ions in both phases in a rather wide temperature range (4–5 K in V_2O_3 and 20 K in VO_2). The width of the temperature range depends on the width of the grain size distribution of the film, since SMPT occurs in grains of different sizes at different temperatures.

Conclusion

This work provides a detailed comparison of the mechanisms of SMPT in sesquioxide (V_2O_3) and vanadium dioxide (VO_2). The comparison is based on the analysis of both experimental data obtained by the authors and the data described in scientific literature. In addition to this, a number of points regarding the SMPT mechanism are described for the first time, such as the two types of π-bonds that can arise in V_2O_3, as well as the new types of π-dimers and σ-dimers that can appear. For the first time, the integrated Mott-Peierls character of SMPT in V_2O_3 has been demonstrated and the causes of near SMPT acoustic emission in both oxides were revealed. The reasons for the difference in the numerical values of the conductivity jumps during SMPT in both oxides have been outlined.

A comparative analysis of the SMPT mechanisms in vanadium oxides expands the possibilities of the practical use of vanadium oxide film structures, as it allows the construction of combined systems for memorization, processing, and storing digital information. Such devices will be of a higher quality than older devices due to the reduction of thermal noise at low SMPT temperatures. In addition, detailed information on the SMPT mechanisms in nanocrystallites of vanadium oxide films will improve the synthesis of thin-film vanadium oxide structures that use the martensitic nature of SMPT in practical devices.

References

Aliev, R. A., Andreev, V. N., Kapralova, V. M. et al. (2006) Vliyanie razmera zeren na fazovyj perekhod metall–poluprovodnik v tonkikh polikristallicheskikh plenkakh dioksida vanadiya [Effect of grain size on the metal–semiconductor phase transition in thin polycrystalline films of vanadium dioxide]. *Fizika tverdogo tela — Physics of the Solid State*, 48 (5), 874–879. (In Russian)

Andreev, V. N., Klimov., V. A., Kompan, M. E. (2017) Fazovyj perekhod metall–dielektrik v gidrirovannykh tonkikh plenkakh V_2O_3 [Metal–insulator phase transition in hydrogenated V_2O_3 thin films]. *Fizika tverdogo tela — Physics of the Solid State*, 59 (12), 2413–2415. DOI: 10.21883/FTT.2017.12.45241.174 (In Russian)

Andreev V. N., Pikulin V. A., Frolov D. I. (2000) Akusticheskaya emissiya pri fazovom perekhode v monokristallakh polutoraokisi vanadiya [Acoustic emission during a phase transition in single crystals of vanadium sesquioxide]. *Fizika tverdogo tela — Physics of the Solid State*, 42 (2), 322–325. (In Russian)

Fan, F., Liu, Y., Li, J., Wang, X.-H., Chang, S.-J. (2015) Active terahertz directional coupler based on phase transition photonic crystals. *Optics Communications*, 336, 59–66. DOI: 10.1016/j.optcom.2014.09.068 (In English)

Gatti, M., Bruneval, F., Olevano, V., Reining, L. (2007) Understanding correlations in vanadium dioxide from first principles. *Physical Review Letters*, 99 (26), article 266402. DOI: 10.1103/PhysRevLett.99.266402 (In English)

Golubev, V. G., Davydov, V. Yu., Kartenko, N. F. et al. (2001) Phase transition-governed opal–VO_2 photonic crystal. *Applied Physics Letters*, 79 (14), 2127–2129. DOI: 10.1063/1.1406144 (In English)

Ilinskiy, A. V., Castro, R. A., Pashkevich, M. E., Shadrin, E. B. (2020) Dielektricheskaya spektroskopiya i osobennosti mekhanizma fazovogo perekhoda poluprovodnik–metall v plenkakh VO_2 [Dielectric spectroscopy and the semiconductor–metal phase transition mechanism in doped VO_2 films]. *Fizika i teknnika poluprovodnikov — Semiconductors*, 54 (2), 153–159. DOI: 10.21883/FTP.2020.02.48910.9267 (In Russian)

Ilinskiy, A. V., Kvashenkina, O. E., Shadrin, E. B. (2011) Metallizatsiya gidrirovaniem monoklinnoj fazy v plenkakh VO_2 [Protonic metallization of monoclinic phase in VO_2-films]. *Fizika i teknnika poluprovodnikov — Semiconductors*, 45 (9), 1197–1202. (In Russian)

Keller, G., Held, K., Eyert, V., Vollhardt, D., Anisimov, V. I. (2004) Electronic structure of paramagnetic V_2O_3: Strongly correlated metallic and Mott insulating phase. *Physical Review B: Covering Condensed Matter and Materials Physics*, 70 (20), article 205116. DOI: 10.1103/PhysRevB.70.205116 (In English)

Lu, Z., Zhao, W. (2012) Nanoscale electro-optic modulators based on graphene-slot waveguides. *Journal of the Optical Society of America. Series B*, 29 (6), 1490–1496. DOI: 10.1364/JOSAB.29.001490 (In English)

McBride, S. L., Hutchison, T. S., Murphy, R. (1974) Acoustic emission and the semiconductor — metal transition in vanadium dioxide thin films. *Scripta Metallurgica*, 8 (4), 431–434. DOI: 10.1016/0036-9748(74)90149-5 (In English)

Mott, N. F. (1990) *Metal-insulator transitions.* 2nd ed. London: Taylor and Francis, 286 p. DOI: 10.1002/crat.2170260620 (In English)

Nagaosa, N., Sinova, J., Onoda, S., MacDonald, A. H., Ong, N. P. (2010) Anomalous hall effect. *Reviews of Modern Physics*, 82 (2), 1539–1592. DOI: 10.1103/RevModPhys.82.1539 (In English)

Schilbe, P. (2002) Raman scattering in VO_2. *Physica B: Condensed Matter*, 316–317, 600–602. DOI: 10.1016/S0921-4526(02)00584-7 (In English)

Shimazu, Y., Okumura, T., Tsuchiya, T. et al. (2015) Metal–insulator transition of c-axis-controlled V_2O_3 thin film. *Journal of the Physical Society of Japan*, 84 (6), 64701–64705. DOI: 10.7566/JPSJ.84.064701 (In English)

Tan, X., Yao, T., Long, R. et al. (2012) Unraveling metal-insulator transition mechanism of VO_2 triggered by tungsten doping. *Scientific Reports*, 2, article 466. DOI: 10.1038/srep00466 (In English)

Tselev, A., Lavrik, N. V., Kolmakov, A., Kalinin, S. V. (2013) Scanning near-field microwave microscopy of VO_2 and chemical vapor deposition graphene. *Advanced Functional Materials*, 23 (20), 2635–2645. DOI: 10.1002/adfm.201203435 (In English)

Wegkamp, D., Stähler, J. (2015) Ultrafast dynamics during the photoinduced phase transition in VO_2. *Progress in Surface Science*, 90 (4), 464–502. DOI: 10.1016/j.progsurf.2015.10.001 (In English)

Ye, H., Wang, H., Cai, Q. (2015) Two-dimensional VO_2 photonic crystal selective emitter. *Journal of Quantitative Spectroscopy and Radiative Transfer*, 158, 119–126. DOI: 10.1016/j.jqsrt.2015.01.022 (In English)

Formation of Δ⁰-izobar in nC-collisions at 4.2 GeV/c

R. N. Bekmirzaev[⊠1], X. U. Bekmirzaeva[1], G. U. Khudoyberdiev[1],
M. I. Mustafayeva[1], B. I. Nabiev[1]

[1] Jizzax State Pedagogical Institute, 4 Sh. Rashidov Str., Jizzax 100130, Uzbekistan

Authors

Rahmatillo N. Bekmirzaev, e-mail: bekmirzaev@mail.ru

Xursand U. Bekmirzaeva

Gulmurod U. Khudoyberdiev

Marjona I. Mustafayeva

Bahodir E. Nabiev

Abstract. The study is dedicated to the multiplicity of momentum and angular characteristics of protons formed in nC-collisions at a pulse of 4.2 GeV/c. The experimental results on the formation of Δ⁰ isobars in nC-collisions at 4.2 GeV/c are presented for the first time. Experimental and normalised background distribution of the effective mass for protons and π⁻-mesons was obtained. This study is a follow-up to prior research. It explores various kinematic characteristics of π⁻-mesons formed in nC-collisions at 4.2 GeV/c. The data obtained are compared with the experimental data obtained for pA interactions at the same energy. The experimental material used in this work was obtained using a 2-meter propane bubble chamber of the JINR LHE irradiated with beams of proton, deuteron and helium-4 nuclei at a pulse of 4.2 GeV/c per nucleon at the Dubna Synchrophasotron and consists of 6736 pC, 7071 dC and 11974 ⁴HeC events. Negative π mesons are identified visually by the charge sign only.

Keywords: hadron and nucleus-nucleus collisions, Δ⁰-isobar, π⁻-mesons, effective proton masses, accelerator, propane chamber, carbon.

Introduction

It is well known that so far there is no theory of strong interactions available. Here, an important role is played by the study of multiple processes where many secondary-charged and neutral particles are formed in inelastic hadron-nucleus and nucleus-nucleus interactions in a wide energy range. To obtain useful information, it is necessary to analyse processes where many nucleons are involved in the interaction. To date, quite a lot of material has been accumulated on the interactions of protons with nucleons and nuclei in a wide range of primary energies. Monochromatic neutron beams are difficult to obtain; therefore, experimental information on neutron collisions with nuclei (nA) obtained under conditions of the 4π geometry is scarce (Iqbal et al. 2014) and supported with little statistical data. In this regard, obtaining experimental data on nA collisions and comparing them with experimental data obtained at the same energy for the same target nucleus is of significant interest. One of the fundamental tasks in modern nuclear physics is the study of non-nucleon degrees of freedom. In the beginning, the proton-neutron composition of the nucleus was discovered followed by quasi-nucleons, pions, baryon resonances, partons, quarks and gluons.

As for baryon resonances, the relevance of Δ resonance formation remains an important research topic, both experimentally and theoretically. This is due to the fact that Δ resonances can be formed in various strong and electromagnetic interactions under the influence of various particles—pions, baryons, nuclei, γ-quanta and electrons. Moreover, not all existing theoretical models allow a unique description of the total experimental data on the generation of Δ resonance. The results obtained in this work showed that characteristics (width and mass) of the Δ resonance generated in nuclear collisions differ from those of the Δ resonance generated in free nuclear collisions.

Experiment

This study is a follow-up to prior research (Iqbal et al. 2014). It explores various kinematic characteristics of π⁻-mesons formed in nC-collisions at a pulse of 4.2 GeV/c. The data obtained are compared with the experimental data obtained for pA interactions at the same energy. The experimental material used in this study was obtained using a 2-meter propane bubble chamber of the JINR LHE irradiated with beams of proton, deuteron and helium-4 nuclei at a pulse of 4.2 GeV/c per nucleon at the Dubna Synchrophasotron and consists of 6736 pC, 7071 dC and 11974 ⁴HeC events. Negative π mesons are identified visually by the sign of the charge only. The admixture of unidentifiable electrons among them does not exceed 5%, while negative strange particles do not exceed 1%. The lower boundary of the pulse which allows certain identification of the charged pions is 70 MeV/c.

Methodological features of the experiment regarding corrections for the loss of secondary charged particles are given in (Nakamura et al. 2010). In contrast to (Olimov et al. 2011; Olimov et al. 2007), this work takes into account the contributions to the impulse characteristics of the secondary π⁻-mesons with less than 4 cm projection length of the tracks. Only emission angles and, naturally, their impulses for a short projection length of tracks in the working volume of the camera were measured for such π mesons. The momenta restoration of such π⁻-mesons was carried out as follows. Pulse spectra of π⁻-mesons with a projection length of tracks greater than 4 cm were constructed. Each spectrum was divided into 18 histograms according to their emission angle θ $(0 \leq \theta \leq 180°)$ in a laboratory system with an angular interval width $\Delta\theta=10°$.

Then, according to the measured departure angle of π⁻-mesons with less than 4 cm track projection length, the value of their momentum was played randomly by one of the pulsed histograms. Interactions of neutrons with carbon nuclei were distinguished from collisions of deuterons and ⁴He nuclei with carbon nuclei by the presence of a stripping proton or a ³He nucleus in these events, respectively. The average multiplicities of π⁻-mesons in nC events isolated from dC and ⁴HeC collisions coincided within the statistical error, being 0.72 ± 0.02 and 0.70 ± 0.03, respectively. The average values of the total momenta of π⁻-mesons in nC events obtained from dC and ⁴HeC collisions turned out to be 0.59 ± 0.01 GeV/c and 0.59 ± 0.02 GeV/c, respectively, coinciding with one another. We also note the coincidence within the statistical error of the average transverse momenta of the π⁻-mesons in nC events obtained from dC and ⁴HeC collisions, which amounted to 0.25 ± 0.01 GeV/c and 0.24 ± 0.01 GeV/c, respectively. From the above facts, the average values of the escape angles of π⁻-mesons in nC events isolated from dC and ⁴HeC collisions coincide. Further analysis of the momentum and angular distributions of π-mesons was carried out for the combined group of nC events in the laboratory system.

Figure 1 shows the experimental and background distribution of the effective mass for protons and π⁻-mesons in nC collisions. The experimental distribution over the invariant mass of the pairs $(p\pi^-)$ was obtained by combining protons and pions in each individual experimental event. The background distribution over the invariant mass of pairs $(p\pi^-)$ was obtained by combining protons and pions selected randomly from different events. Figure 1 shows that the experimental spectrum dn/dM for most pairs $(p\pi^-)$ contains a large contribution from uncorrelated pairs of protons and pions. Experimental distributions were obtained using a set of developed criteria by combining protons and π⁻-mesons in each individual event. Background distributions were constructed according to the same criteria as the experimental distributions, but protons and pions were selected randomly from different events.
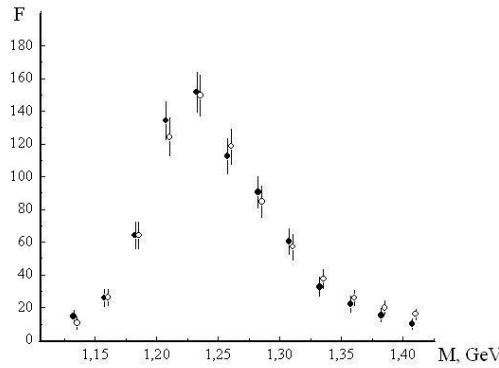
Fig. 1. The experimental and background distribution of the effective mass for protons and π⁻-mesons in nC-collisions

The isolation of Δ^0 isobars was performed in accordance with the procedure given in (Olimov et al. 2012). Figure 1 shows the experimental and normalised background distribution of the effective mass for protons and π⁻-mesons

$$F(M) = \frac{CM\Gamma M_\Delta}{(M^2 - M^2_\Delta)^2 + \Gamma^2 M^2_\Delta},$$

where M_Δ and Γ are the mass and the width of the resonance. A set of distributions $D(M)$ for various parameters ε and a values was fixed by the Breit-Wigner function and a value was found for each fit. The parameters M_Δ and Γ were determined by minimising the difference $|D(M) - b(M)|$. Figure 2 shows that the spectrum is well described by this formula with values $M = 1226 \pm 7$ MeV/c² and $\Gamma = 83 \pm 14$ MeV. In this case, the fraction of π⁻-mesons from the decay of Δ^0 isobars turned out to be $36 \pm 4\%$. This result coincides within the statistical error with the data of (Olimov et al. 2012) and also indicates a 1.45-fold decrease in the width of Δ^0 isobars in the nucleus compared to the collisions of free nucleons.
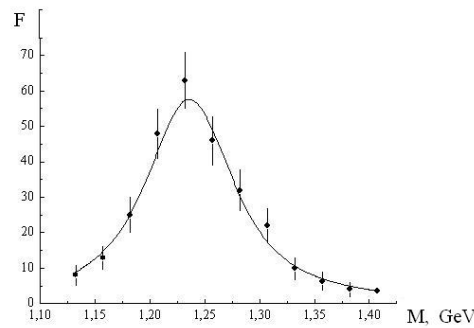

Fig. 2. The spectrum described by the formula with M = 1226 ± 7 MeV/c² and Γ= 83 ± 14 MeV

Conclusion

A comparative analysis of the pulsed and angular spectra of π⁻-mesons in pC and nC events was carried out. The analysis showed that there is no additional production of π⁻-mesons on the carbon nucleus in comparison to nucleon-nucleon interactions at a primary pulse of 4.2 GeV/c per nucleon. The pulsed and rapid spectra of π⁻-mesons for pC and nC collisions differ in the entire variation range

of these quantities. At the same time, the transverse momentum distributions are almost identical for the types of interactions discussed, which may be due to the fact that the transverse momentum transferred is identical to the carbon core for pC and nC collisions.

References

Iqbal, A., Olimov, K. K., Khan, I., Yuldashev, B. S., Haseeb, M. Q. (2014) On centrality and rapidity dependences of transverse momentum spectra of negative pions in ^{12}C + ^{12}C collisions at 4.2 GeV/c per nucleon. *International Journal of Modern Physics E: Nuclear Physics*, 23 (09), article 1450047. DOI: 10.1142/S0218301314500475 (In English)

Nakamura, K., Hagiwara, K., Hikasa, K. et al. (Particle data group) (2010) Review of particle physics. *Journal of Physics G: Nuclear and Particle Physics*, 37 (7), article 075021. DOI: 10.1088/0954-3899/37/7A/075021 (In English)

Olimov, K., Lutpullaev, S. L., Olimov, Kh. K. et al. (2011) Production of multibaryon clusters in hadron-nucleus collisions at high energies. *Physics of Atomic Nuclei*, 74 (1), 98–102. DOI: 10.1134/S1063778811010121 (In English)

Olimov, Kh. K., Lutpullaev, S. L., Olimov, K., Gulamov, K. G., Olimov, J. K. (2007) Production of Δ⁰ and Δ⁺⁺ resonances in collisions of ^{4}He nuclei with carbon nuclei at 4.2 GeV/c per nucleon. *Physical Review C: Covering Nuclear Physics*, 75 (6), article 067901. DOI: 10.1103/PhysRevC.75.067901 (In English)

Olimov, Kh. K., Haseeb, M. Q., Khan, I., Olimov, A. K., Glagolev, V. V. (2012) Δ⁰ (1232) production in d + ^{12}C collisions at 4.2 A GeV/c. *Physical Review C: Covering Nuclear Physics*, 85 (1), article 014907. DOI: 10.1103/PhysRevC.85.014907 (In English)